Quasi 3D electronic structures of Dion-Jacobson layered perovskites with exceptional short interlayer distances.

Maria Maniadi, Nicolas Mercier, Alla Skorokhod, Maroua Ben Haj Salah, Pierre Bidaud, Piétrick Hudhomme, Claudio Quarti, Wei Li, David Beljonne, Jacky Even, et al.

J. Mater. Chem. C 2023, https://pubs.rsc.org/en/content/articlelanding/2023/tc/d3tc03807f
DOI: 10.1039/D3TC03807F

Quasi 3D electronic structures of Dion-Jacobson layered perovskites with exceptional short interlayer distances

Maria Maniadi,[a,b] Nicolas Mercier,[a]*Alla Skorokhod,[a] Maroua Ben Haj Salah,[a] Pierre Bidaud,[a] Piétrick Hudhomme,[a] Claudio Quarti,[c]* Wei Li,[c,†] David Beljonne,[c] Jacky Even,[d] Claudine Katan,[e] Constantinos C. Stoumpos[b]
Maria Maniadi,[a,b] Nicolas Mercier,[a]*Alla Skorokhod,[a] Maroua Ben Haj Salah,[a] Pierre Bidaud,[a] Piétrick Hudhomme,[a] Claudio Quarti,[c]* Wei Li,[c,†] David Beljonne,[c] Jacky Even,[d] Claudine Katan,[e] Constantinos C. Stoumpos[b]

[a] MOLTECH Anjou, UMR-CNRS 6200, Univ Angers, 2 Bd Lavoisier, 49045 Angers, France, e-mail: nicolas.mercier@univ-angers.fr
[b] Department of Materials Science and Technology, University of Crete, Heraklion 70013, Greece.
[c] Laboratory for Chemistry of Novel Materials, Materials Research Institute, University of Mons-UMONS, Place du Parc 20, Mons B-7000, Belgium, e-mail: claudio.quarti@umons.ac.be
[d] Univ Rennes, INSA Rennes, CNRS, Institut FOTON - UMR 6082, F-35000 Rennes, France.
[e] Univ Rennes, ENSCR, INSA Rennes, CNRS, ISCR (Institute des Sciences Chimiques de Rennes), UMR 6226, France.
† Current address: School of Chemistry and Materials Science, Hunan Agricultural University, Changsha 410128, People's Republic of China
Electronic Supplementary Information (ESI) available: [details of any supplementary information available should be included here]. See DOI: 10.1039/x0xx00000x

Abstract. In the field of perovskite solar cells (PSCs), 3D/2D heterostructures are a promising route to obtain highly efficient and stable devices. Herein, inspired by dications which have afforded rare layered perovskites called Dion-Jacobson (DJ), with short interlayer distances, we designed and synthesized the new 2-iodopropane-1,3-diamonium dication (DicI), and we successfully obtained multi-n 2D layered perovskites $(DicI)(MA)_{n-1}Pb_nI_{3n+1}$ (n= 1-4, MA^+= methylammonium). As a result of a suitable size of the dication which well fits, in projection to the layer planes, in the square defined by four adjacent apical iodides, as well as halogen bonding between organic iodine and apical iodides ($I_{(ap)}$) of perovskite layers, a perfect eclipsed configuration between adjacent layers takes place, yielding unprecedented short $I_{(ap)}\ldots I_{(ap)}$ distances, as small as 3.882 Å in $(DicI)(MA)_2Pb_3I_{10}$. Density Functional Theory (DFT) calculations highlight unusually strong valence band dispersion along the the $\Gamma \rightarrow Z$ direction. Effective masses for out-of-plane motions of holes are estimated on par with values computed for 3D perovskites, and similar to in-plane effective masses in 2D multilayered perovskites. This indicates these layered compounds feature quasi 3D electronic structures, hence appearing as promising candidates for PSCs heterostructures.

Introduction. Halide perovskites are rapidly emerging as ideal candidates for the development of efficient and inexpensive photovoltaic technology. Still, devices based on these materials present major stability issues, with T_{99}, defined as the time over which 99% of the initial photovoltaic efficiency is preserved, often lying in the range of few days or even hours. The fabrication of 3D/2D perovskite thick bilayer stacks has been recently proposed as a suitable solution to lessen the stability bottleneck, with demonstration of an excellent photovoltaic efficiency of 24.5% along with exceptional stability with T_{99} >2000 hours (3D perovskite: $APb(I_{0.90}Br_{0.10})_3$ -A= Cs, FA, MA-; 2D perovskite: $BA_2MA_2Pb_3I_{10}$ -BA= butylammonium-).[1] This result demonstrates that thick 3D/2D heterostructures shall inherit the intrinsic durability of 2D perovskites, showing the huge interest of this class of materials for decisive progresses toward the industrialization of halide perovskite photovoltaic technology. The counterpart of the stability of 2D perovskites is the ineffective charge and energy transport perpendicular to the perovskite sheet, stemming from the interruption of the metal halide chemical connectivity along one direction. It may yield strong performance limitations in 3D/2D heterostructures based on thick 2D layers, even in situations where flat valence band alignments are favorable for hole extraction.[1] One way to overcome this issue is to obtain a perfect flip of the stacking axis of the 2D layer, as demonstrated in a few cases for 2D PSCs.[2] But applying the same growth engineering process in a perfect way appears to be more challenging in the context of 3D/2D heterostructures.[1] Alternatively, enhancing the transport along the stacking axis through

J. Mater. Chem. C 2023, https://pubs.rsc.org/en/content/articlelanding/2023/tc/d3tc03807f
DOI: 10.1039/D3TC03807F

chemical engineering of the interlayer was one of the motivations leading in 2018 to the discovery of Dion-Jacobson multilayered halide perovskites.[3]

The 2D A^+ (n>1 perovskite prototype is based on B_nX_{3n+1} perovskite network incorporating small organic cations) separated by either long size monocations (A'^+) or dications (A''^{2+}). This leads to the following formula: $(A')_2(A)_{n-1}B_nX_{3n+1}$ and $(A'')(A)_{n-1}B_nX_{3n+1}$ (<100> series according to the Mitzi's classification),[4-6] with n measuring the number of BX_6 octahedra along the thickness of the individual 2D inorganic sheet. The size and conformation of the A'^+ or A''^{2+} spacers directly affect the interlayer distance, which in turn impacts the interlayer transport properties. These are also influenced by the relative shift between adjacent layers (usually measured as fraction of metal-metal distance), with eclipsed (0,0) configuration guaranteeing the most effective overlap between the orbitals of apical iodides, compared to staggered (1/2, 1/2) in plane displacement, for a given interlayer separation. Except a rare case where a A'^+ monocation can lead to eclipsed situation with quite short I…I distance (4.27 Å in $(HO(CH_2)_2NH_3)_2PbI_4$),[7] the few 2D perovskites exhibiting an eclipsed situation with close I…I contacts (<4.30 Å) are based on short A''^{2+} dications.[3, 8, 9] Such perovskites are classified as DJ (Dion-Jacobson) perovskites.[10] It has been shown that close I…I distances can lead to strong dispersion for both the valence and conduction electronic bands. Moreover, it has been demonstrated that a light-activated interlayer contraction occurs in such perovskites boosting the photovoltaic efficiency of a perovskite solar cells (PSCs) based on a phase pure 2D multi-layered perovskite active layer, from 15 % to 18%.[11] Furthermore, thick (n=3,4) 2D perovskites also feature smaller exciton binding energies and ideal valence band matching with parental 3D compounds, leading to efficient hole extraction in PSCs.[11] Overall, the search for such new layered perovskites with short interlayer separation and that sustain the formation of multi-n compounds is of great interest for technological applications.[1] Thus far, only a few dications have afforded multilayered DJ compounds. The cyclic 4AMP (4-(aminomethyl)piperidinium, Scheme 1)[3] and 4AMPY (4-(aminomethyl)pyridinium)[8] dications have four carbon atoms separating the two ammonium ends and form multi-n (n=1,4) 2D layered perovskites with eclipsed (0, 0) stacking motif and short I…I distance. Notice that four carbon alkylated $^+H_3N(CH_2)_4NH_3^+$ dication was also successfully incorporated into a 2D halide perovskite but only for the thinner n=1 $A''PbI_4$ structure.[12] The shortest dications stabilizing DJ phases reported to date have three carbon atoms between ammonium ends: 3AMP (3-(aminomethyl)piperidium),[3] 3AMPY (3-(aminomethyl)pyridinium)[8] and mPDA (*m*-phenylenediammonium,[9] Scheme 1). Noteworthy, the linear diammonium dication $^+H_3N(CH_2)_3NH_3^+$, while leading to a n=1 $PbCl_4$ perovskite network, does not afford Pb_nI_{3n+1} network based hybrid compounds.[13] In this context we have designed and synthesized a derivative dication $^+H_3NCH_2CH(I)CH_2NH_3^+$ (named $DicI^{2+}$, Scheme 1). The substitution of a hydrogen atom by an iodine atom has several advantages. The iodine atom leads to a bulkier dication than $^+H_3N(CH_2)_3NH_3^+$, which should allow, as for mPDA or 3AMP, the formation of DJ compounds. In addition, as demonstrated recently by some of us for multilayered perovskites based on the $I(CH_2)_2NH_3^+$ monocation, weak electronic hybridization takes place between the iodine from the organic with those from the inorganic lattice, which enhances the interlayer electronic coupling although the quite long I_{ap}….I_{ap} distance of 6.1 Å.[14] Herein, we report the synthesis of the 2-iodopropane-1,3-diamonium dication ($DicI^{2+}$), and the layered perovskites $(DicI)(MA)_{n-1}Pb_nI_{3n+1}$ (n= 1-4, MA^+= methylammonium), a rare series of DJ perovskites. In fact, due to both a suitable size of $DicI^{2+}$ cations and halogen bonding between iodine atoms of $DicI^{2+}$ and apical iodides ($I_{(ap)}$) of the perovskite layers, a perfect eclipsed situation of adjacent layers takes place, and unprecedent short $I_{(ap)}$….$I_{(ap)}$ distances are observed. For these compounds, density functional theory (DFT) calculations anticipate sizeable valence band dispersion along the direction perpendicular to layers, leading to small effective masses for out-of-plane motions of holes, similar to usual in-plane effective masses. Although less pronounced, a similar effect is also predicted for electrons. Hence, this multi-n series of 2D perovskites exhibits a quasi 3D like electronic band structure and these DJ compounds appear as good candidates for PSCs applications, both as active material or in 3D/2D bilayer stacks.

DOI: 10.1039/D3TC(

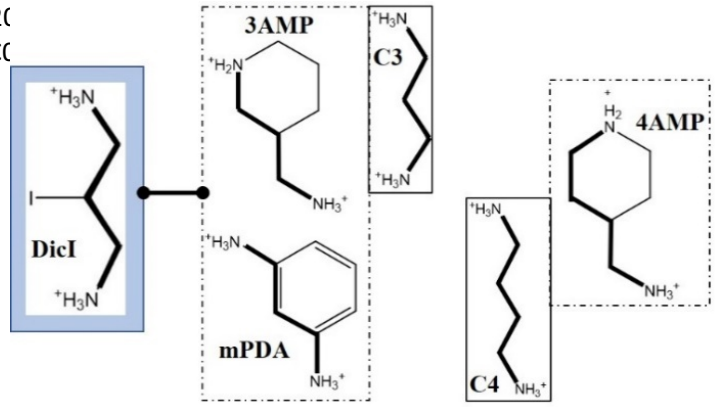

Scheme 1. The targeted $DicI^{2+}$ dication and selected dications that have afforded DJ multilayered perovskites based on three (3AMP, mPDA) or four (4AMP) carbon atoms separating ammonium ends (the linear diammonium cations $^{+}H_3N(CH_2)_mNH_3^{+}$-m= 3 (C3), 4 (C4)- are drawn for comparison) (the two other cations affording DJ phases, 3AMPY and 4AMPY have conjugated rings compared to 3AMP and 4AMP)

Results and Discussion. The synthesis of the 2-iodopropane-1,3-diamonium diodide ($(DicI)I_2$) has been carried out in three steps from the commercial 1,3- aminopropan-2-ol molecule which has been recently incorporated in lead deficient 3D perovskites.[15] The amino groups of 1,3- aminopropan-2-ol are first protected using di-tert-butyl dicarbonate (Boc_2O) leading to the di-tert-butyl (2-hydroxypropane-1,3-diyl)dicarbamate compound as a white solid in quantitative yield (Scheme S1 and Fig. S1, details in SI). The introduction of the mesylate leaving group was then carried out using methane sulphonyl chloride in the presence of triethylamine in 83% yield. The obtained white solid was treated with a HI solution and heated at 75°C over night. Both deprotection of Boc amino protecting groups and nucleophilic substitution of the mesylate group by the iodide anion could occur simultaneously. Finally, the addition of ethyl acetate caused the precipitation of the expected $(DicI)I_2$ salt which was isolated in 86% yield. The 2-iodopropane-1,3-diammonium dication ($DicI^{2+}$) was characterized by ^{1}H and ^{13}C NMR spectra (Fig S1). The n= 1 compound $(DicI)PbI_4$ is obtained as red, plate-like crystals from a slow cooling of a HI solution containing the metal precursor (PbI_2) and the dication salt $(DicI)I_2$ in 1/1 ratio (see SI). For both n=2 and n=3 compounds, the reaction was non-stoichiometric using the spacer ($DicI^{2+}$) as the limiting reagent. In a first vial, the dication salt is dissolved in HI under constant heating (~130 ^{o}C) while in a second one, the metal precursor (PbO) is first added in HI giving a clear yellow solution before the slow addition of methyammonium iodide (MAI). Then the content of the first vial was added, the reaction mixture being left under reflux for 10-15 minutes. The solution was left to cool slowly to ambient temperature, using the glass cover to maintain the equilibrium conditions. A day later, scarlet, plate like crystals (n=2) and nearly black, plate like crystals (n=3), were obtained as pure phases (see details in Exp. part) as revealed by X-ray powder diffraction (XRD, Fig. S2) and optical characterizations. Interestingly, the above procedure is an efficient and conveniently used method in order to obtain the 2D perovskite members (n = 2, 3) in their pure phase, which cannot be obtained when the reaction is done using stoichiometric ratio. All the n=1-3 compounds are stable up to 215°C and no thermal accident occurs in the RT-175°C range (see TGA and DSC curves, Fig. S4).

A general view of the crystal structures of the $(DicI)(MA)_{n-1}Pb_nI_{3n+1}$ (n = 1-4) compounds is shown in Fig. 1 (see also Fig. S3a). Detailed crystallographic data are provided in the Supporting Information (Tables S1-3). The n=1 and n=2 compounds crystallize in the centrosymmetric space group Cmce and Pbam, respectively, while the n=3 and n= 4 perovskites are described in the non-centrosymmetric space group Aea2 and Pba2, respectively. The short $DicI^{2+}$ dication involves an eclipsed configuration of consecutive adjacent layers along the stack axis, as illustrated for the n= 1 compound (Fig. 1, inset).

J. Mater. Chem. C 2023, https://pubs.rsc.org/en/content/articlelanding/2023/tc/d3tc03807f
DOI: 10.1039/D3TC038

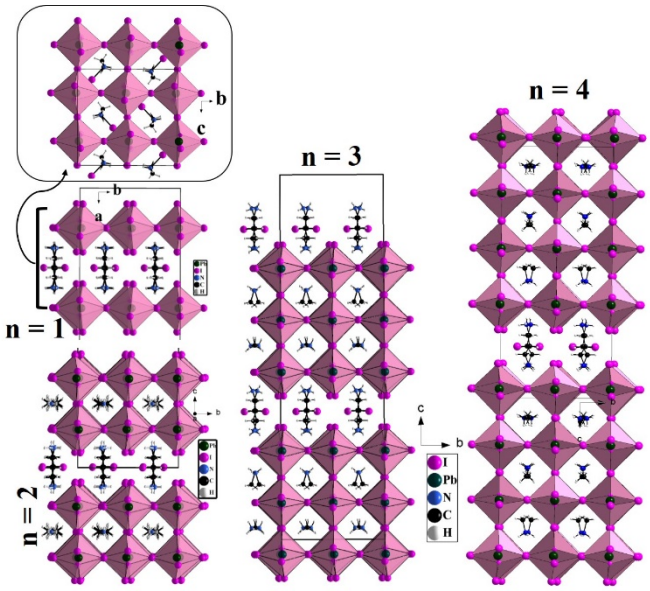

Fig. 1 General view of crystals structures of $(DicI)(MA)_{n-1}Pb_nI_{3n+1}$ (n= 1-4) along the layers plane. For the n= 1 compound, a partial view along the *a* axis -perpendicular to layers- of two adjacent layers is also provided as inset revealing their eclipsed stacking and the position of $DicI^{2+}$ cations in the interlayer space.

As shown in Fig. 2a, only ammonium heads of dications are localized within the perovskite sheet. This is known to induce a tilt of PbI_6 octahedra leading to out-of-plane distortions. For $(DicI)PbI_4$ (n= 1), we clearly observe that, if half equatorial iodides are contained in planes defined by Pb atoms, the other half are out of these planes (Fig. 1). The distortions of a perovskite layer can be illustrated by the Pb-I(eq)-Pb bond angles (eq= equatorial). For n= 1, these angles are of 180° along b (Pb and I(eq) in planes) and 143° along c. For the multilayered compounds (n= 2-4), the outer layers as well as the inner layers (n= 3, 4) display similar out-of-plane tilt, the Pb-$I_{(eq)}$-Pb bond angles being in the 145-180° range with average values of 161.5° (n=1), 158.3° (n= 2), 160.9° (n= 3) and 162.4° (n=4) (see details in Table S3). As regards to Pb-$I_{(ax)}$-Pb bond angles (ax= axial, see Fig. S3b), they are close to 160° for all n= 2-4 compounds (Table S3). Octahedra belonging to the n= 1 compound and to the inner layers of the n= 3 and n= 4 compounds are quite regular (Pb-I bond distances in the 3.17-3.22 Å (n= 1), 3.10-3.20 Å (n= 3) or 3.14-3.18 Å and 3.13-3.23 Å ranges (n= 4)). In contrast, octahedra of the n= 2 compound as well as those belonging to the outer layers of the n=3 and n= 4 perovskites appear more distorted (Pb-I bond distances in the 3.07-3.27 Å (n= 2), 3.03-3.33 Å and 3.07-3.24 Å (n= 3), 3.04-3.33 Å and 3.05-3.30 Å (n= 4) ranges).

Not only the $DicI^{2+}$ dication affords the formation of these $(DicI)(MA)_{n-1}Pb_nI_{3n+1}$ multilayered perovskites of DJ type where an eclipsed situation of adjacent layers occurs, but it leads to unprecedented short $I_{(ap)}$…$I_{(ap)}$ distances. The figure 2a shows the $I_{(ap)}$…$I_{(ap)}$ and $I_{(ap)}$….$I_{(orga)}$ interactions ($I_{(ap)}$: apical iodide of perovskite layers; $I_{(orga)}$: iodine of $DicI^{2+}$) at the organic-inorganic interface of the $(DicI)(MA)_2Pb_3I_{10}$ compound. Organic halogens are known to be involved in halogen bonding interactions.[16, 17] The origin of this electrostatic interaction comes from the anisotropy of the electron density around the organic halogen nucleus, which can be represented by an ellipsoid elongated in the direction across the C-X bonding axis. Thus, a Lewis base (B) such as iodide could interact with the electron-deficient region of X (ideal C-X….B bond angle of 180°), while a Lewis acid (A) could interact with the electron-rich region of X (ideal C-X….A bond angle of 90°). In the structure of $DicI^{2+}$ based perovskites, as illustrated in $(DicI)(MA)_2Pb_3I_{10}$, the organic iodine atom interacts with two iodides of adjacent layers, the C-I…$I_{(ap)}$ distances being approximately 3.90 Å which is less than twice the van der Waals radius of I (4.0 Å), and the C-I….$I_{(ap)}$ bond angles is 149.4° which deviates from the ideal value of 180°.

J. Mater. Chem. C 202 3/tc/d3tc03807f
DOI: 10.1039/D3TC03

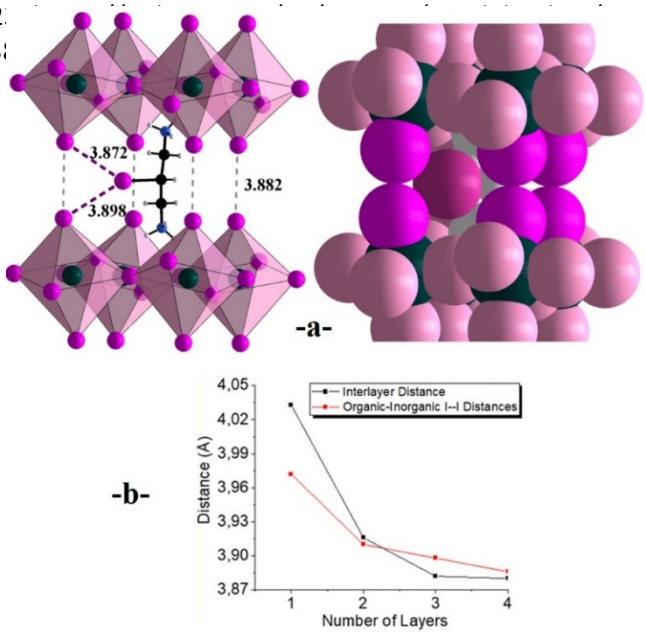

Fig. 2 a) Partial view of the structure of $(DicI)(MA)_2Pb_3I_{10}$ showing the $I_{(ap)}\ldots I_{(ap)}$ and $I_{(ap)}\ldots I_{(orga)}$ interactions ($I_{(ap)}$: apical iodide of perovskite layers; $I_{(orga)}$: iodine of $DicI^{2+}$; distances in Å) at the organic-inorganic interface : ball and stick (left) and space-filling (I radius of 1.98 Å, right) representations; b) $d(I_{(ap)}\ldots I_{(ap)})$ and $d(I_{(ap)}\ldots I_{(orga)})$= f(n) in $(DicI)(MA)_{n-1}Pb_nI_{3n+1}$ (n= 1-4).

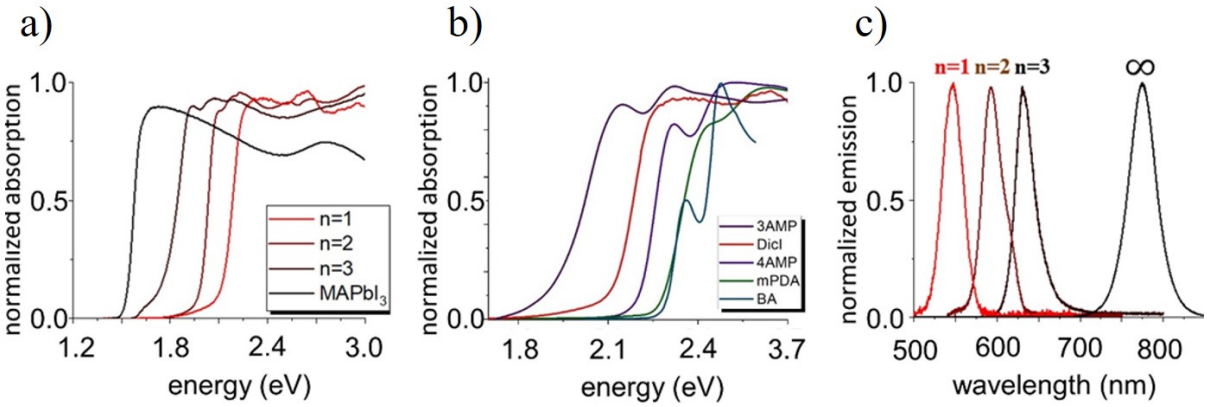

Fig. 3 (a) Optical absorption of the (DicI)(MA)n-1PbnI3n+1 perovskites (n = 1, 2, 3) and ¬MAPbI3, obtained from diffuse reflectance measurements converted using the Kubelka−Munk function (α/S = (1 − R)2 /2R). (b) Reflectance spectra of (DicI)PbI4 (n=1) 2D halide perovskite, compared to similar measurements reported in the literature for other n=1 compounds: 3AMP, 4AMP, (Reprinted with Permission from Ref. 3) mPDA (Reprinted with Permission from Ref. 9) and BA (Reprinted with Permission from Ref. 19). Copyright American Chemical Society. (c) Photoluminescence spectra of n=1-3 and ¬MAPbI3 (n = ∞) obtained from a micro-PL setup (lexc =532nm) for 0.4mW laser power and a 1µm laser beam radius.

Table 1. $I_{(ap)}\ldots I_{(ap)}$ and $I_{(ap)}\ldots I_{(orga)}$ distances in $(DicI)(MA)_{n-1}Pb_nI_{3n+1}$ (n= 1-4) and in selected DJ perovskites.

Dication	Layered perovskite	$I_{(ap)}\ldots I_{(ap)}$ distance (Å)	$I_{(ap)}\ldots I_{(orga)}$ distance (Å)
$DicI^{2+}$	$(DicI)PbI_4$	4.033	3.972
	$(Dic)(MA)Pb_2I_7$	3.916	3.910
	$(Dic)(MA)_2Pb_3I_{10}$	3.882	3.898
	$(Dic)(MA)_3Pb_4I_{13}$	3.880	3.886
$3AMP^{2+}$	$(3AMP)(MA)_2Pb_3I_{10}$	4.021	-
$4AMP^{2+}$	$(4AMP)(MA)_2Pb_3I_{10}$	4.105	-
$mPDA^{2+}$	$(mPDA)(MA)_2Pb_3I_{10}$	3.988	-
H_2BDA^{2+}	$(H_2BDA)PbI_4$	4.285	-

J. Mater. Chem. C 2023, https://pubs.rsc.org/en/content/articlelanding/2023/tc/d3tc03807f
DOI: 10.1039/D3TC03807F

As a result of the short size of $DicI^{2+}$ dication as well as C-I….$I_{(ap)}$ interactions, a very short $I_{(ap)}…I_{(ap)}$ distance of 3.882 Å is encountered in $(DicI)(MA)_2Pb_3I_{10}$. The space filling representation of the figure 2a especially highlights all these weak interactions at the organic-inorganic interface. Table 1 lists the shortest $I_{(ap)}…I_{(ap)}$ and $I_{(ap)}…I_{(orga)}$ distances observed in the $(DicI)(MA)_{n-1}Pb_nI_{3n+1}$ series as well as shortest $I_{(ap)}…I_{(ap)}$ distances found in some selected DJ perovskites based on short dications: 3AMP,[3] 4AMP,[3] mPDA[9] and H_2BDA.[12] It appears that the $I_{(ap)}…I_{(ap)}$ observed in n= 3 and n= 4 compounds of the $(DicI)(MA_{n)-1}Pb_nI_{3n+1}$ series are the shortest one among the set and, to the best of our knowledge, the shortest ever reported. Sizeable electronic communication in the direction perpendicular to layers is thus anticipated (vide infra). Interestingly, both $I_{(ap)}…I_{(ap)}$ and $I_{(ap)}….I_{(orga)}$ distances decrease with increasing thickness of the perovskite layer, from n=1 to n= 4 (Fig. 2b). For $I_{(ap)}…I_{(ap)}$, a similar trend has been observed with 3AMP (4.187 Å to 3.999 Å from n= 1 to n= 4),[3] 4AMP (4.211 Å to 4.103 Å from n= 1 to n= 4),[3] and mPDA (4.273 Å to 3.988 Å from n= 1 to n= 3).[9]

More, the new DicI-based DJ series is in a favourable situation for the formation of multilayered compounds, thanks to a small negative lattice mismatch with the 3D reference $MAPbI_3$ structure (see Supporting Information and Fig. S6), which limits the accumulation of strain energy for intermediate n-values.[18] This is in favour of stable higher n-values compositions, especially with methylammonium as perovskitizers, given that $MAPbI_3$ has no instability towards a thermodynamic δ-phase.

In sight of their potential application in photovoltaics, we characterized the optical properties of these compounds, performing diffuse reflectance measurements between 185-1400 nm (UV-vis-NIR spectroscopy) and photoluminescence (PL) spectroscopy (Fig. 3). The diffuse reflectance measurements at room temperature (Fig. 3a) can't resolve the exciton absorption from the bandgap absorption. However, the compounds exhibit steep absorption edges from which the optical band-gap can be set at 2.12 eV, 1.98 eV, 1.76 eV and 1.55 eV, for n=1-3 and $MAPbI_3$, respectively, as evaluated from steep absorption onset (see Fig. S5). Consistently, the 3D $MAPbI_3$ compound exhibits the lowest energy gap (n=∞ layers). The impact of shorter $I_{(ap)}…I_{(ap)}$ distances on optical band gaps in DicI based DJ perovskites compared to other DJ perovskites is difficult to estimate because the distortions of perovskite layers, which are very different in all these materials, have also a strong impact on band gaps. The spectra of n= 1 layered perovskites based on $DicI^{2+}$, $3AMP^{2+}$, $4AMP^{2+}$, $mPDA^{2+}$ and BA^{+} cations are shown in Fig. 3b. Although a longer apical iodide distance, one compound, $(3AMP)PbI_4$ (d= 4.187 Å), exhibits a lower energy absorption band than $(DicI)PbI_4$ (d= 4.033 Å) which can be explained by strong out-of-plane distortions in the latter compared to the former. Photoluminescence properties of specimens obtained from all n compounds, as shown in Fig. 3c, were measured at room temperature using a confocal microscope setup with a steady-state excitation source (532 nm). The photoluminescence emission energy of the series of multilayered perovskites decreases with increasing layer thickness, hence paralleling the trend in absorption. The photoluminescence spectra consist of one single emission peak for each of the compounds corresponding to the absorption spectra. A sharp, weak PL emission was observed for all of the compounds at 550 nm, 593 nm and 630 nm, for n=1, 2 and 3, respectively. This is the signature of efficient energy relaxation processes of charge carriers through the perovskite electronic band structures and down to the emitting edge states.

We further investigated the electronic properties of newly reported $(DicI)(MA)_{n-1}Pb_nI_{3n+1}$ series, by performing periodic DFT calculations. To this aim, we considered the structural models retrieved from single-crystal XRD analysis (Fig. 1) and performed partial optimization of the organic component. This allows to preserve the structural details for the inorganic lattice evinced from the previous analyses. To ease the comparison of the band dispersion and avoid complications raising from their different Bravais lattices (see Table S1), we described all n=1,4 $(DicI)(MA)_{n-1}Pb_nI_{3n+1}$ compounds within a conventional primitive orthorhombic lattice. In addition, we rotated the axes, with the plane stacking direction now matching the c-axis, so that the reciprocal direction associated to the plane stacking corresponds in all cases to Γ→Z. Band dispersion are calculated using the PBE exchange-correlation potential, including Spin-Orbit-Coupling (SOC). This approach is known to underestimate the single-particle band gap of 2D halide perovskites but provides consistent trends for different compounds and effective masses in reasonable agreement with the experiments, and was widely employed in the past (details about the employed software and the computational set-up can be found in the Supporting Information).[6, 20-23]

J. Mater. Chem. C 2023, https://pubs.rsc.org/en/content/articlelanding/2023/tc/d3tc03807f
DOI: 10.1039/D3TC03807F

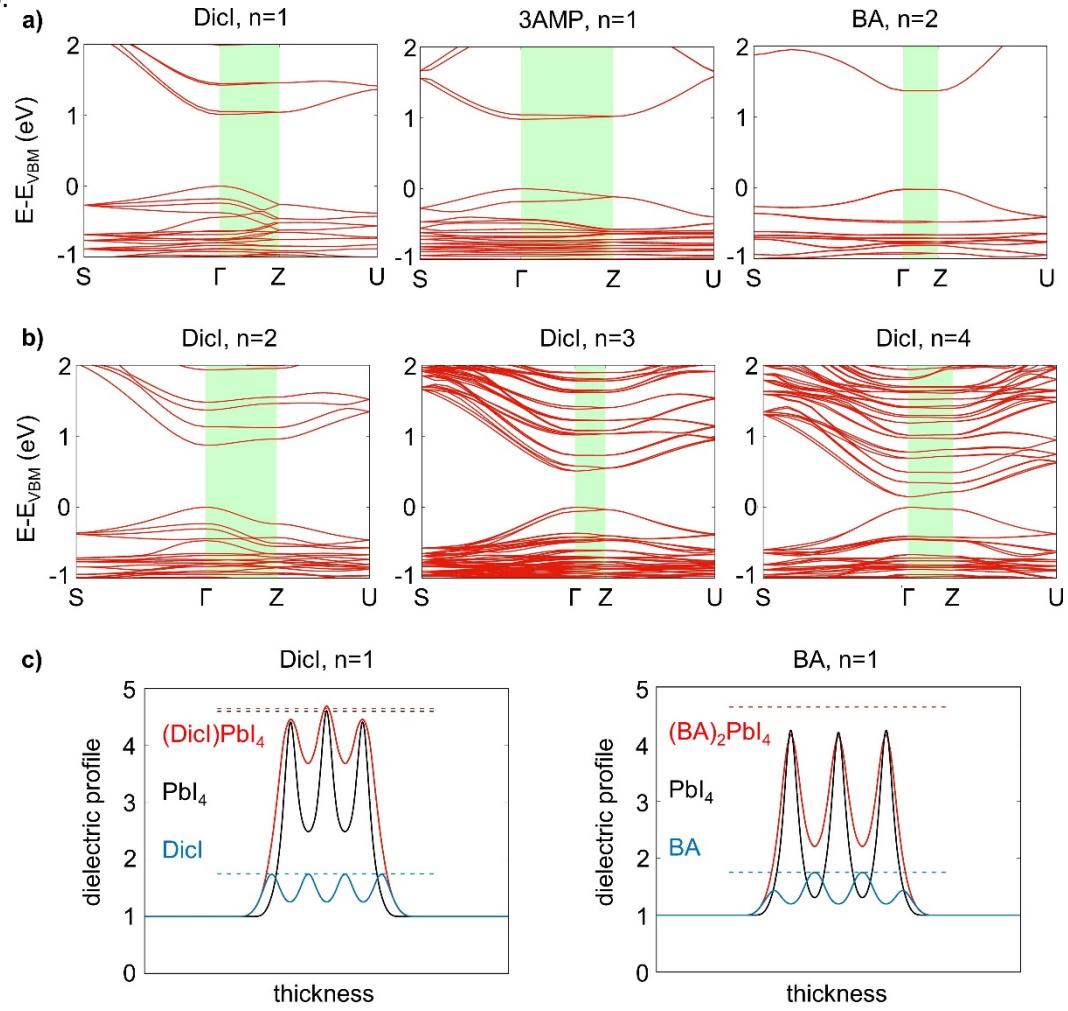

Fig. 4 (a) Band dispersion for n=1, (DICl)PbI_4 2D halide perovskite, compared with corresponding band dispersion in reference (3AMP)PbI_4 and $(BA)_2PbI_4$ halide perovskite; the highlighted area is associated to the dispersion in the plane stacking direction. (b) Band structure dispersion for n=2-4 (DICl)$(MA)_{n-1}Pb_nI_{3n+1}$ 2D halide perovskites. (c) Dielectric profile computed for the (DICl)PbI_4 and $(BA)_2PbI_4$ 2D halide perovskites. Dielectric profiles are shown for the full compounds (red line) and for the composing inorganic PbI_4 frame (black line) and organic spacers (DICl and BA, blue line), as obtained following the composite approach described in Ref.[24]. Horizontal dashed lines are common to the two graphs and to ease the comparison between the dielectric profiles.

Band structure for n=1 (DICl)PbI_4 compound is shown in Figure 4a, compared to that of other two n=1 reference compounds, namely, widely-studied butylammonium (BA^+),[19, 21, 23] and ($3AMP^{2+}$).[3] Most notably, while $(BA)_2PbI_4$ shows flat dispersion along the Γ→Z direction associated to the plane stacking, both (3AMP)PbI_4 and (DICl)PbI_4 exhibit significant band dispersion, especially in the valence region, indicating effective interlayer communication and anticipating sizeable vertical hole transport. Band dispersion of (DICl)PbI_4 in the Γ→Z direction is very similar to that of (3AMP)PbI_4 halide perovskite, whose n=3 analogue recently demonstrated 18% efficiency performance in pure 2D PSCs.[11] Conduction band is comparably much less dispersed, as was previously explained on the basis of symmetry allowed atomic hybridization.[25] While the valence band maximum features a contribution from the p_z orbitals of the apical iodines (p_z being the p-orbital polarized along the plane stacking direction), the conduction band minimum features a contribution only from the p_{xy} orbitals of the apical iodines, whose orientation does not allow for an effective mix of the Bloch states of adjacent layers. Band dispersion for n=2-4 compounds are illustrated in Fig. 4b, showing progressive reduction of the band gap with increasing the thickness of the inorganic frame, as due to corresponding reduction of the quantum confinement.[6] One may notice that increase in the inorganic layer thickness is accompanied by a progressive decreases in the valence band maximum and opposite increase in

the dispersion in the conduction band minimum. Nevertheless, the comparison of the band dispersion for different compounds should be taken with care. First, because many structural details contribute to determine the band dispersion, as the tilting of the octahedra, the crystal lattice parameters and the number of the inorganic layers per unit cell (band folding for the n=1,3 compounds), the latter even influencing the interpretation of the bands themselves. Furthermore, increased band dispersion with compound thickness should not be straightly associated with enhanced interlayer mobility. It may indeed indicate the case where the electronic conjugation is enhanced within the individual inorganic Pb_nI_{3n+1} sheet, due to reduced quantum confinement, with interlayer interactions remaining unaffected. Band dispersion within all the first Brillouin zone are reported in the Supporting Information (Fig. S7), with thicker n= 3,4 showing Rashba induced spin-splitting of the bands, consistently with the loss of inversion symmetry.[26] Modelling charge transport in 2D halide perovskites is a very challenging task not achieved yet in the literature, as these materials likely sustain different in- and out-of-plane transport mechanisms in a very anharmonic lattice. Still, effective masses as estimated from the curvature of the frontier levels may serve as a useful descriptor to clarify vertical transport properties in these compounds, as compared to other references from the literature.[14, 22, 27-29] For (DicI)PbI_4, we estimated out-of-plane hole/electron effective masses of 0.25/1.54, which are much smaller than those of $(BA)_2PbI_4$ and reach values surprisingly close to those reported for in-plane directions.[14, 22, 29] Noteworthy, a sizeable reduction by a factor of 2 of the hole effective mass is predicted by comparison with (3AMP)PbI_4 (0.25 versus 0.5). (DicI)PbI_4 vertical electron effective masses are close to those of (3AMP)PbI_4 (1.34). These small estimates for the effective masses should be first understood in terms of the short interlayer distance, with the planes passing for the apical iodides separated by 6.7 Å and 3.9 Å for $(BA)_2PbI_4$ and (DicI)PbI_4, respectively. Additionally, the advantageous eclipsed motif characteristic of the DJ prototype also contributes in maximizing the overlap between atomic orbitals. Full list of charge effective masses along the plane stacking direction are reported in the Supporting Information (Table S4). We also estimated the dielectric function profile of (DicI)PbI_4 compound along the plane stacking direction, together with $(BA)_2PbI_4$ compound, taken as reference (Fig. 4c). The procedure for the estimation of the dielectric profile is taken from Ref. 26 and is performed considering three inorganic layers and the spacers requested to preserve charge neutrality (the procedure is detailed in the Supporting Information). Interestingly, the dielectric constant of the central inorganic layer of the (DicI)PbI_4 compound is 0.5 larger than that of $(BA)_2PbI_4$. In addition, also the minima of the profile, associated with the organic spacer, increase from 2.2 to 3.7, overall indicating a reduction of the dielectric contrast. To assess the cause of this difference, we further computed the dielectric profile of the sole inorganic and organic components, as computed separately, and found that the organic profile is very close for the two materials. The reduction of the interlayer distance lies therefore at the origin of the reduced dielectric confinement in (DicI)PbI_4. This in turn may anticipate some reduction of the exciton binding energy which may ease dissociation of excitons in this compound.

On the other hand, one may wonder whether the $DicI^{2+}$ spacer does contribute to the small effective mass values. In a previous work by some of us, we showed that iodine atomic states from iodo-ethylammonium spacer are partially involved in the formation of the frontier levels of the inorganic frame and contribute to the reduced out-of-plane effective mass in those 2D compounds.[14] In that case, the iodine-containing spacer acted as mediator in the vertical charge transport, compared to the usual direct hybridization of the Bloch states from the two separated layers. To understand whether $DicI^{2+}$ has a similar role, we performed additional DFT simulations by substituting the iodine in the spacer with bromine, chlorine or hydrogen, and computed corresponding $\Gamma \rightarrow Z$ dispersion and effective masses. This substitution leads to some changes in the corresponding band structure (see Fig. S8), in particular in the spacing between the VBM and deeper states in the valence, at Γ. The latter may be conceptually associated with the interplanar interactions, as following the band folding due to the presence of two layers per cell. Nevertheless, the impact in terms of hole effective mass, as related to the curvature of the top valence band, is minimal (0.25, 0.24, 0.24 for Br, Cl and H, respectively) hence suggesting the spacer does not play a similar mediating role as the iodo-ethylammonium spacer.[14] This, however, should be considered in line with the exceptionally small effective masses of the DicI-based compounds, stemming from the very short interlayer distance of the present compounds (3.9 Å) compared to that found in iodine-ethylammonium based 2D halide perovskites (6.1 Å).

J. Mater. Chem. C 2023, https://pubs.rsc.org/en/content/articlelanding/2023/tc/d3tc03807f
DOI: 10.1039/D3TC03807F

In other words, in the present case, the electronic coupling between adjacent layers is so effective that the contribution from the organic iodine becomes marginal.

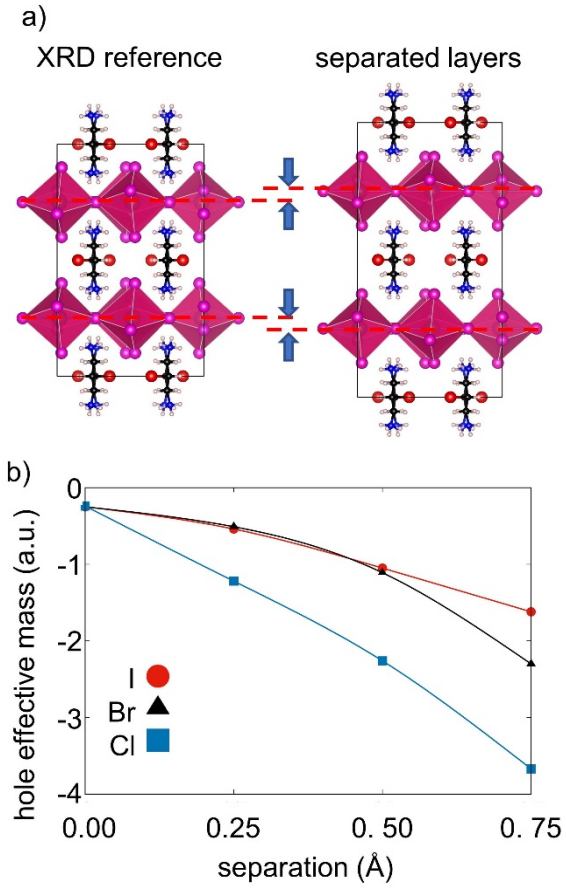

Fig. 5 (a) $DicIPbI_4$ (n=1) models with increased interlayer distances; b) corresponding hole effective masses, with the halide from the cation corresponding to iodine, bromine and chlorine.

To better illustrate this concept, we performed a computational experiment, where we progressively expanded the cell in the plane stacking direction and we increased the interlayer separation (Fig. 5a). This should weaken the direct coupling from adjacent layers, so to make emerge the potential influence of the indirect interaction associated to the halide from the spacer. We hence recomputed the effective hole mass, with the spacer incorporating either a iodine, a bromine or a chlorine, finding indeed that the increase of the interlayer separation leads to heavier effective masses, as expected from less effective overlap of the atomic orbitals (Fig. 5b). Nevertheless, the decrease is faster for the chlorine than for the bromine and from the iodine, paralleling the spatial extension of the outer electronic shell of these atoms, hence highlighting the indirect role played by the halide from the spacer. Total energy differences also suggest that the halide from the spacer has a role in the thermodynamic stabilization of the 2D perovskite frame. Separation of the layers as from Fig. 5a in fact leads to a decrease of the total energy of the system which however depends on the halide from the spacer. In particular, the thermodynamic cost of introducing an interlayer separation of 0.75 Å is larger when with DicI spacer (0.76 eV/chem.u.) than for DicBr (0.73 eV/chem.u./0.75 Å) or a DicCl (0.70 eV/chem.u./0.75 Å).

Conclusion. In this work, we report on the synthesis of the 2-iodopropane-1,3-diamonium dication ($DicI^{2+}$) and the synthesis and characterization of a rare series of 2D DJ layered perovskites, $(DicI)(MA)_{n-1}Pb_nI_{3n+1}$ (n= 1-4). Due to both a suitable size of $DicI^{2+}$ cations and halogen bonding between organic iodine and apical iodides ($I_{(ap)}$) of perovskite layers, a perfect eclipsed situation of adjacent layers takes place, and unprecedent short $I_{(ap)}\cdots I_{(ap)}$ distances (<3.90 Å) are observed. The optical band-gap of the pure n= 1-3 compounds have been estimated to 2.12 eV, 1.98 eV and 1.76 eV from diffuse reflectance measurements. DFT calculations

highlight significant valence band dispersion along the Γ→Z direction perpendicular to layers, and effective masses of out-of-plane hole/electron have been estimated at 0.25/1.54 for the prototype compound (DicI)PbI_4. These values which are similar to usual in-plane effective masses, are much smaller than those of $(BA)_2PbI_4$ and, for holes, smaller than those of other DJ perovskites (0.50 for (3AMP)PbI_4). This indicates these multilayered compounds feature quasi 3D electronic structure especially for hole transport, hence appearing as very good candidates for 2D materials in perovskite solar cells.

Author Contributions. The manuscript was written through contributions of all authors. All authors have given approval to the final version of the manuscript.

Conflicts of interest. There are no conflicts to declare

Acknowledgements. The work at ISCR and MOLTECH-Anjou was mainly supported by the Agence Nationale pour la Recherche (MORELESS project). C. K. and J. E. acknowledge funding from the European Union's Horizon 2020 program, through an Innovation Action under Grant Agreement No. 861985 (PeroCUBE). The present research benefited from computational resources made available on Lucia, the Tier-1 supercomputer of the Walloon Region, infrastructure funded by the Walloon Region under the grant agreement n°1910247. W.L. acknowledges financial support of Wallonie-Bruxelles International (WBI) Excellence scholarship. D. B is FNRS research director. C.Q. is FNRS research associate. This work received financial support under the EUR LUMOMAT project and the Investments for the Future program ANR-18-EURE-0012 for P.B. as Master LUMOMAT student. CCS acknowledges support from the Special Account for Research Funding of the University of Crete under grant KA10652.

Notes and references

1 S. Sidhik, Y. Wang, M. De Siena, R. Asadpour, A. J. Torma, T. Terlier, K. Ho, W. Li, A. B. Puthirath, X. Shuai, A. Agrawal, B. Traore, M. Jones, R. Giridharagopal, P. M. Ajayan, J. Strzalka, D. S. Ginger, C. Katan, M. A. Alam, J. Even, M. G. Kanatzidis, A. D. Mohite, *Science* **2022**, *377*, 1425-1430 doi:10.1126/science.abq7652.

2 H. Tsai, W. Nie, J.-C. Blancon, C. C. Stoumpos, R. Asadpour, B. Harutyunyan, A. J. Neukirch, R. Verduzco, J. J. Crochet, S. Tretiak, L. Pedesseau, J. Even, M. A. Alam, G. Gupta, J. Lou, P. M. Ajayan, M. J. Bedzyk, M. G. Kanatzidis, A. D. Mohite, *Nature* **2016**, *536*, 312-316 10.1038/nature18306.

3 L. Mao, W. Ke, L. Pedesseau, Y. Wu, C. Katan, J. Even, M. R. Wasielewski, C. C. Stoumpos, M. G. Kanatzidis, *Journal of the American Chemical Society* **2018**, *140*, 3775-3783 10.1021/jacs.8b00542.

4 D. B. Mitzi, in *Progress in Inorganic Chemistry*, **1999**, pp. 1-121.

5 B. Saparov, D. B. Mitzi, *Chem Rev* **2016**, *116*, 4558-96 10.1021/acs.chemrev.5b00715.

6 C. Katan, N. Mercier, **2019**, *119*, 3140-3192 10.1021/acs.chemrev.8b00417.

7 N. Mercier, S. Poiroux, A. Riou, P. Batail, *Inorganic Chemistry* **2004**, *43*, 8361-8366 10.1021/ic048814u.

8 X. Li, W. Ke, B. Traoré, P. Guo, I. Hadar, M. Kepenekian, J. Even, C. Katan, C. C. Stoumpos, R. D. Schaller, M. G. Kanatzidis, *Journal of the American Chemical Society* **2019**, *141*, 12880-12890 10.1021/jacs.9b06398.

9 L. Gao, X. Li, B. Traoré, Y. Zhang, J. Fang, Y. Han, J. Even, C. Katan, K. Zhao, S. Liu, M. G. Kanatzidis, *Journal of the American Chemical Society* **2021**, *143*, 12063-12073 10.1021/jacs.1c03687.

10 N. Mercier, *Angewandte Chemie International Edition* **2019**, *58*, 17912-17917 https://doi.org/10.1002/anie.201909601.

11 S. Sidhik, Y. Wang, M. De Siena, **2022**, *377*, 1425-1430 10.1126/science.abq7652.

12 A. Lemmerer, D. G. Billing, *CrystEngComm* **2012**, *14*, 1954-1966 10.1039/C2CE06498G.

13 A. B. Corradi, A. M. Ferrari, G. C. Pellacani, A. Saccani, F. Sandrolini, P. Sgarabotto, *Inorganic Chemistry* **1999**, *38*, 716-721 10.1021/ic980893k.

14 A. Skorokhod, C. Quarti, A. Abhervé, M. Allain, J. Even, C. Katan, N. Mercier, *Chemistry of Materials* **2023**, *35*, 2873-2883 10.1021/acs.chemmater.2c03718.

15 L. Gollino, A. Leblanc, J. Dittmer, N. Mercier, T. Pauporté, *ACS Omega* **2023**, *8*, 23870-23879 10.1021/acsomega.3c02292.

16 G. Cavallo, P. Metrangolo, R. Milani, T. Pilati, A. Priimagi, G. Resnati, G. Terraneo, *Chemical Reviews* **2016**, *116*, 2478-2601 10.1021/acs.chemrev.5b00484.

17 J. Lieffrig, O. Jeannin, M. Fourmigué, *Journal of the American Chemical Society* **2013**, *135*, 6200-6210 10.1021/ja400740v.

18 M. Kepenekian, B. Traore, **2018**, *18*, 5603-5609 10.1021/acs.nanolett.8b02078.

19 C. C. Stoumpos, D. H. Cao, D. J. Clark, J. Young, J. M. Rondinelli, J. I. Jang, J. T. Hupp, M. G. Kanatzidis, *Chemistry of Materials* **2016**, *28*, 2852-2867 10.1021/acs.chemmater.6b00847.
20 J. Even, L. Pedesseau, M. A. Dupertuis, J. M. Jancu, C. Katan, *Physical Review B* **2012**, *86*, 205301 10.1103/PhysRevB.86.205301.
21 A. Fraccarollo, V. Cantatore, G. Boschetto, L. Marchese, M. Cossi, *The Journal of Chemical Physics* **2016**, *144*, 10.1063/1.4947305.
22 C. Quarti, N. Marchal, D. Beljonne, *The Journal of Physical Chemistry Letters* **2018**, *9*, 3416-3424 10.1021/acs.jpclett.8b01309.
23 J. C. Blancon, A. V. Stier, H. Tsai, W. Nie, C. C. Stoumpos, B. Traoré, L. Pedesseau, M. Kepenekian, F. Katsutani, G. T. Noe, J. Kono, S. Tretiak, S. A. Crooker, C. Katan, M. G. Kanatzidis, J. J. Crochet, J. Even, A. D. Mohite, *Nature Communications* **2018**, *9*, 2254 10.1038/s41467-018-04659-x.
24 J. Even, L. Pedesseau, M. Kepenekian, *Physical Chemistry Chemical Physics* **2014**, *16*, 25182-25190 10.1039/C4CP03267E.
25 C. Quarti, C. Katan, J. Even, *Journal of Physics: Materials* **2020**, *3*, 10.1088/2515-7639/aba6f6.
26 M. Kepenekian, R. Robles, C. Katan, D. Sapori, L. Pedesseau, J. Even, *ACS Nano* **2015**, *9*, 11557-11567 10.1021/acsnano.5b04409.
27 Z. Fang, X. Hou, Y. Zheng, Z. Yang, K.-C. Chou, G. Shao, M. Shang, W. Yang, T. Wu, *Advanced Functional Materials* **2021**, *31*, 2102330 https://doi.org/10.1002/adfm.202102330.
28 Z. Xu, M. Chen, S. F. Liu, *The Journal of Physical Chemistry Letters* **2019**, *10*, 3670-3675 10.1021/acs.jpclett.9b01360.
29 M. Dyksik, H. Duim, X. Zhu, Z. Yang, M. Gen, Y. Kohama, S. Adjokatse, D. K. Maude, M. A. Loi, D. A. Egger, M. Baranowski, P. Plochocka, *ACS Energy Letters* **2020**, *5*, 3609-3616 10.1021/acsenergylett.0c01758.

A- Synthesis

A1- Synthesis of 2-iodopropane-1,3-diammonium diodide [(DicI)2+ 2I-

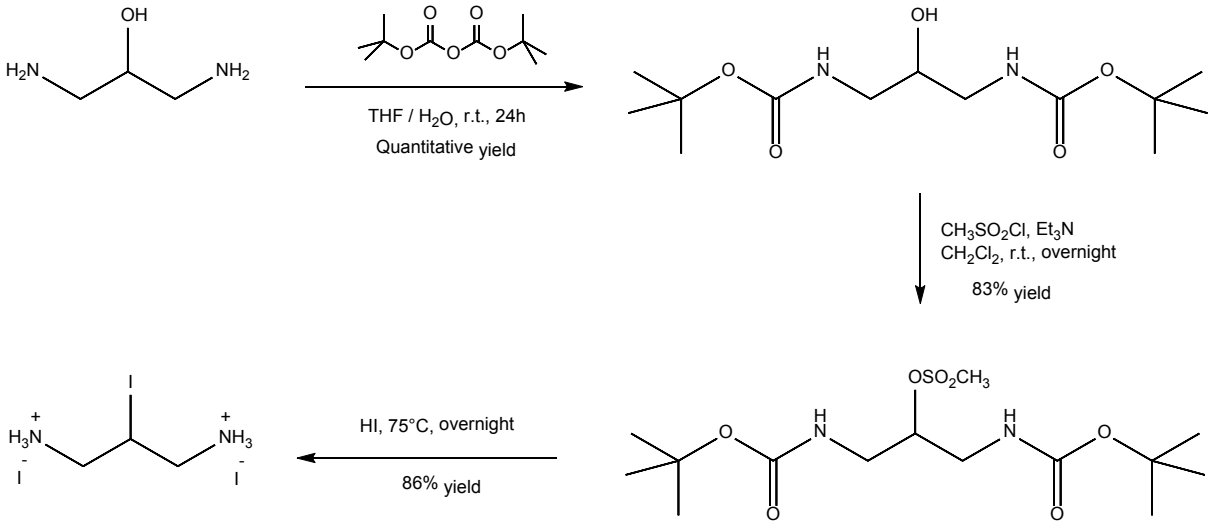

Scheme S1. Synthesis of the (DicI)I2 salt from commercial 1,3- aminopropan-2-ol.

The synthesis of the $(DicI)I_2$ salt from commercial 1,3- aminopropan-2-ol is described on Scheme S1. To a solution of di-tert-butyl dicarbonate (Boc_2O) (5.2 g, 2.4 eq., 24 mmol) in 60 mL THF was added dropwise a solution of 1,3-aminopropan-2-ol (0.90 g, 1 eq., 10 mmol) in 80 mL of THF / H_2O (1/1, v/v) mixture . The solution was stirred for 24 hours at room temperature. The solvent was partially concentrated under reduced pressure to remove THF and the residue was extracted with diethyl ether. The organic layer was washed with brine, then dried with anhydrous magnesium sulphate, filtered and concentrated under reduced pressure. Recrystallisation in a mixture of diethyl ether and petroleum ether afforded after filtration the white solid –(6.90 g) of di-tert-butyl (2-hydroxypropane-1,3-diyl)dicarbamate in quantitative yield.

To a solution of diamino diprotected molecule (0.725 g, 2.5 mmol) in 10 mL of dichloromethane (HPLC purity) was added distilled triethylamine (0.5 mL, 3.75 mmol). The solution is cooled in an ice bath, then methane sulphonyl chloride (0.23 mL, 3 mmol) is added dropwise. After stirring for 24 hours at room temperature under argon atmosphere, 0.5 mL of water was added and the mesylate compound was extracted with dichloromethane. The organic phase was washed with water, then dried with magnesium sulphate, filtered, and concentrated under reduced pressure. Crystallization using a minimum of dichloromethane and petroleum ether afforded after filtration the mesylate compound (0.76 g) in 83% yield.

The mesylate compound (1g, 2.7 mmol) was introduced into a 10 mL flask and HI acid was added till it covered the compound. The system was plugged by a septum into which a needle was inserted i to create the isobar. The solution was left to stir overnight at 75°C. , Ethyl acetate was then added to the reaction mixture and left for 2 hours in order to completely precipitate the 2-iodopropane-1,3-diammonium diodide $[(DicI)^{2+}\ 2I^-]$salt . The compound was filtered and washed with ethyl acetate. The salt was placed in the oven to dry at 70°C for 1 hour and isolated (1.06 g) in 86% yield.

^1H and ^{13}C NMR spectra (Figure S1) were obtained on a 500 MHz Advance III HD spectrometer (500 MHz for ^1H and 125 MHz for ^{13}C). Chemical shifts were reported in ppm according to tetramethylsilane using the solvent residual signal as an internal reference (CD_3OD : δ_H = 3.31 ppm, δ_C = 49.0 ppm).

Coupling constants (*J*) were given in Hz. Resonance multiplicity was described as dd (doublet of doublets), tt (triplet of triplets). Carbon spectra were acquired with a complete decoupling for the proton.
^{1}H NMR (500 MHz, CD_3OD) *d* (ppm) = 4.42 (tt, *J* = 4.3 and 9.7 Hz, 1H, CH-I), 3.60 (dd, *J* = 4.3 and 14.1Hz, 2H), 3.40 (dd, *J* = 9.7 and 14.1 Hz, 2H).
^{13}C NMR (125 MHz, CD_3OD) *d* (ppm) = 46.0 (CH), 21.3 (CH_2).
MS (MALDI-TOF) : Calcd for $C_3H_{11}I_3N_2$: 455.85; found : 454.62 $(M-H)^+$

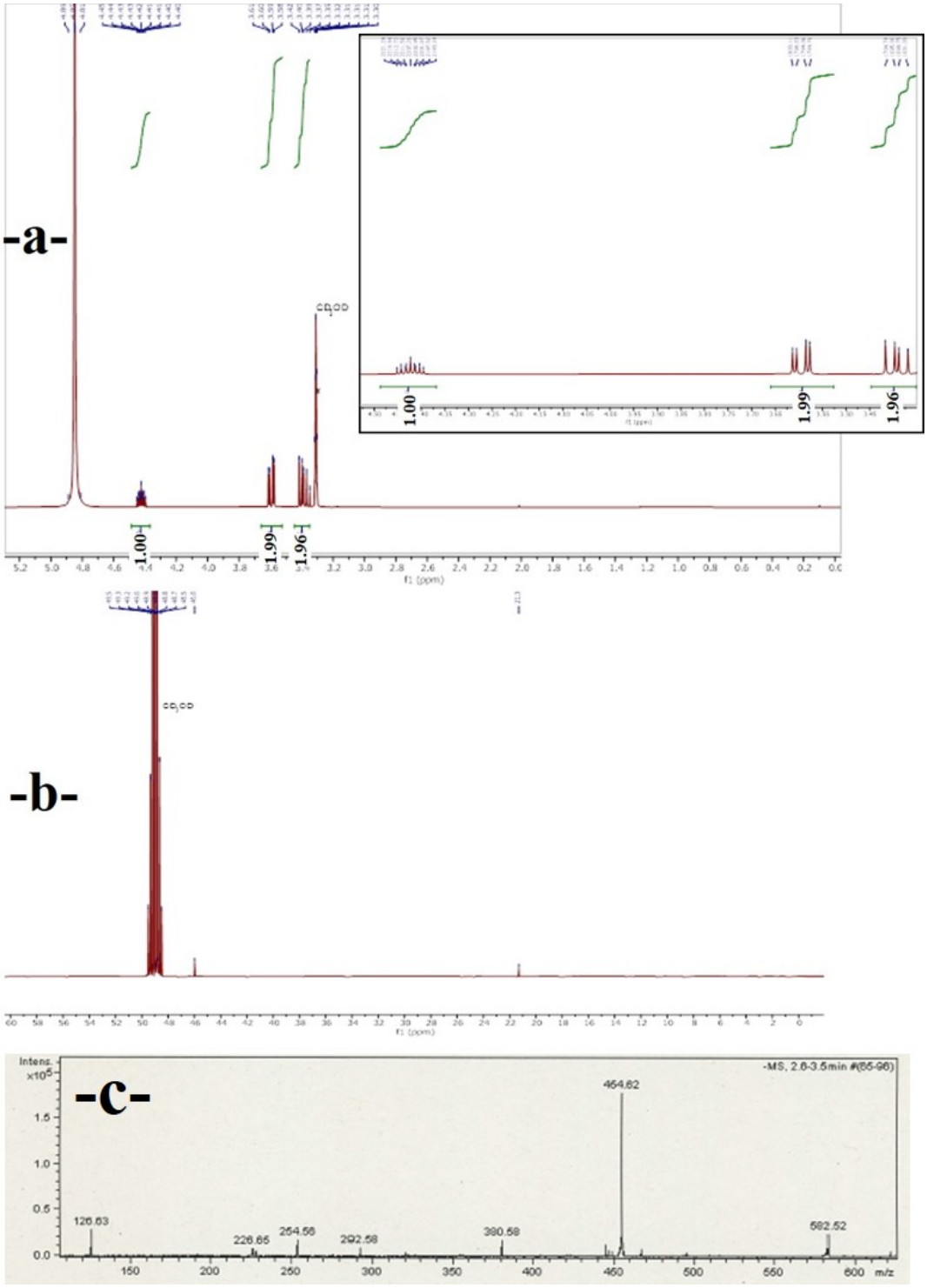

Fig. S1. a) *^{1}H NMR of 2-iodopropane-1,3-diammonium salt in CD_3OD and its enlargment*
b) ^{13}C NMR of 2-iodopropane-1,3-diammonium salt in CD_3OD, c) Mass spectrum (MALDI-TOF) of 2-iodopropane-1,3-diammonium salt

A2- Synthesis of the layered perovskites $(DicI)(MA)_{n-1}Pb_nI_{3n+1}$

PbI_2 (99.9%), PbO (99.9%), hydroiodic acid (57 wt % in H_2O, distilled, stabilized, 99.95%), and hypo phosphorous acid solution (50 wt % in H_2O), and MAI (>99.5%) were purchased from Sigma-Aldrich and used as received.

Synthesis of $(DicI)PbI_4$ (n=1). HI (3mL) and was added to a mixture of PbI_2 (50.0mg, 0.1mmol) and $(DicI)^{2+}$ $2I^-$ (50.0mg, 0.1mmol) in a 20mL scintillation vial, resulting in a mild effervescence (CO_2 emission). The resulting mixture was magnetically stirred to 130℃, resulting in a clear yellow solution. After 30 minutes, stirring was discontinued and the reaction was allowed to cool naturally to ambient temperature. After 30 minutes, red needle-shaped crystals precipitated at the bottom of the vial. The resultant precipitate was isolated via suction filtration and cleaned with ethylene acetate. Yield: 46.8mg (51.09%)

Synthesis of $(DicI)(MA)Pb_2I_7$ (n=2). HI (5mL) and H_3PO_2 (0.5mL) were added in a 20mL scintillation vial of PbO (334.5mg, 1.5 mmol). After 5 minutes of stirring to 130℃, MAI (159.0mg, 1mmol) was added into the dissolved solution, resulting in a clear yellow solution. In another 20mL scintillation vial $(DicI)^{2+}$ $2I^-$ (114.0mg, 0.25mmol) are dissolved in HI (0.5mL) under heating and stirring to 200℃. After, the vial with the (DicI) becomes a clear solution we add its content into the first vial without any significant change in the color of the solution. The resulting mixture was magnetically stirred resulting in a clear yellow solution. We heat the solution at 200℃ until about half of the solvent has evaporated. After 30 minutes, stirring was discontinued and the reaction was allowed to cool naturally to ambient temperature. After 1day, scarlet parallelepiped crystals precipitated at the bottom of the vial. The resultant precipitate was isolated via suction filtration. Yield: 135.8mg (35.35%)

Synthesis of $(DicI)(MA)_2Pb_3I_{10}$ (n=3). HI (4mL) and H_3PO_2 (0.5mL) were added in a 20mL scintillation vial of PbO (446.0mg, 2mmol). After 5 minutes of stirring to 130℃, MAI (318.0mg, 2mmol) was added into the dissolved solution, resulting in a clear yellow solution. In another 20mL scintillation vial $(DicI)^{2+}$ $2I^-$ (45.6mg, 0.1mmol) are dissolved in HI (0.5mL) under heating and stirring to 200℃. After, the vial with the (DicI) becomes a clear solution we add its content into the first vial without any significant change in the color of the solution. The resulting mixture was magnetically stirred resulting in a clear yellow solution. After 30 minutes, stirring was discontinued and the reaction was allowed to cool naturally to ambient temperature. After 1day, dark-red plate-like crystals precipitated at the bottom of the vial. The resultant precipitate was isolated via suction filtration. Yield: 107.5mg (49.8%)

Crystals of $(DicI)(MA)_3Pb_4I_{13}$ (n=4). A process similar to that described for the pure phase of $(DicI)(MA)_2Pb_3I_{10}$ (n=3) involving different PbO/MAI ratios, as for instance 3 mmol/2 mmol, leads to a mixture of n= 3 and n= 4 crystals. A selection of a n=4 single crystal allowed solving its crystal structure from SCXRD data.

B- X-ray diffraction characterization

B1- Powder X-ray Diffraction (PXRD)

The Bruker D8 ADVANCE was used to analyze the powder patterns of the synthesized compounds. It is mounted in the Bragg-Brentano geometry in θ-2θ measurement. The X-rays are formed by a copper anti-cathode of wavelength 1.5406 Å allowing us to obtain a diffractogram of I=f(2θ). The detection angles that measured with this XRD model started from 5º up to 40º. The data collected and analyzed using EVA and OriginPro software, respectively. All experimental XRD patterns seem well fit with the calculated ones obtained from single crystal X-ray data meaning that the n=1, n= 2 and n= 3 compounds are obtained as pure phases (Figure S2). Comparing the powder patterns for n = 1-3, we observe that all patterns exhibit peaks in different angles. For the n=1, a small characteristic peak shows up right before 2θ = 10°, corresponding to the (200) plane, while there is an intense double peak right before 2θ = 16°, corresponding to the (020) and (002) planes, respectively. For n=2, some peaks including the first one (right after 2θ = 5°, corresponding to (001) crystallographic plane), are not observed in the experimental pattern due to their low signal to noise ratio. An intense peak shows up right after 2θ = 10°, corresponding to the (002). We also observe an intense double peak right before 2θ = 15°, corresponding to the (020) and (200) planes. For n=3, we observe a characteristic slightly weak diffraction right before 2θ = 10°, and an intense peak right above the same angle, corresponding to the (004) and (113) planes, respectively. A characteristic double peak is observed at the PXRD of n=3 as well, right before 2θ = 15°, corresponding to the (020) and (115) planes, respectively.

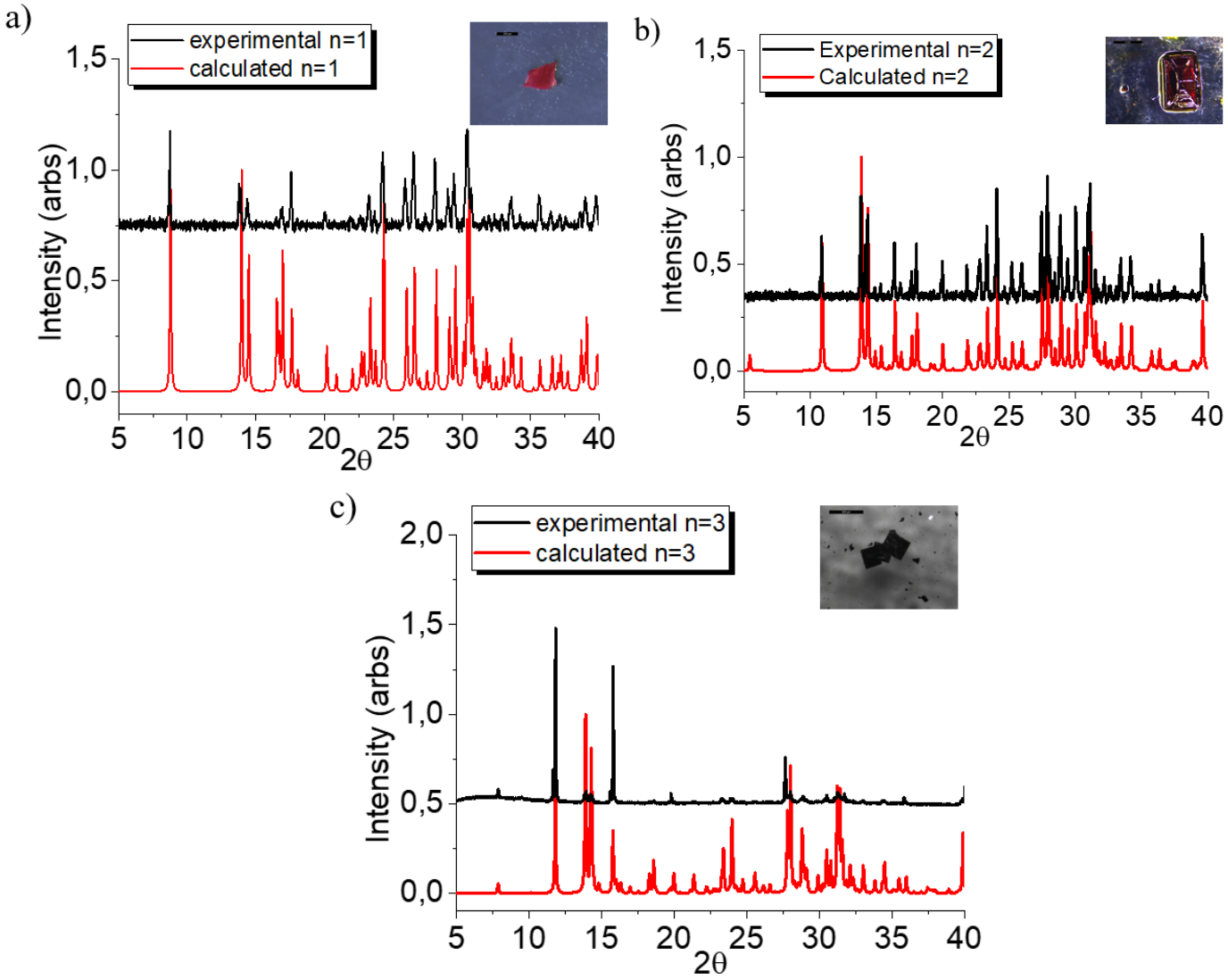

Fig. S2. Powder X-ray diffraction (PXRD) patterns of the experimental a) n=1 b) n=2 and c) n=3 compounds compared to their calculated patterns.

B2- Single crystal X-ray Diffraction (SCXRD)

X-ray diffraction data were collected on a Rigaku Oxford Diffraction SuperNova diffractometer equipped with Atlas CCD detector and micro-focus Cu-K_α radiation (λ = 1.54184 Å). Data were collected at 293 K. Intensities were corrected for Lorentz-polarization effects, as well as for absorption effect (gaussian method using CrysAlisPro program -CrysAlisPro, Rigaku Oxford Diffraction, V1.171.41.118a, 2021). Crystal structures were solved by charge flipping and refined (full-matrix least-squares on F^2) using the Jana2006 package. CCDC numbers are : 2283257 (n= 1), 2283259 (n= 2), 2283265 (n= 4), 2283266 (n= 3).

Table S1. Crystal Data and Structure Refinement for $(DicI)(MA)_{n-1}Pb_nI_{3n+1}$

	$(DicI)PbI_4$	**$(DicI)(MA)Pb_2I_7$**	**$(DicI)(MA)_2Pb_3I_{10}$**	**$(DicI)(MA)_3Pb_4I_{13}$**
Crystal System	orthorhombic	orthorhombic	orthorhombic	orthorhombic
Space Group	C m c e	P b a m	A e a 2	P b a 2
Unit Cell Dimensions				
a (Å)	a = 20.1168(15)	a = 12.3289(8)	a = 12.3926(5)	a = 12.4176(5)
b (Å)	b = 12.6758(10)	b = 12.7636(7)	b = 12.7378(5)	b = 12.7217(5)
c(Å)	c = 12.2263(7)	c = 16.2040(9)	c = 44.8986(15)	c = 28.7245(9)
α (deg)	α = 90	α = 90	α = 90	α = 90
β (deg)	β = 90	β = 90	β = 90	β = 90
γ (deg)	γ = 90	γ = 90	γ = 90	γ = 90
Volume ($Å^3$)	3117.7(4)	2793.813	7087.4(5)	4537.7(3)
Z	8	4	8	4
Density (gr/ cm^3)	3.9067	4.0032	4.0426	4.0646
Independent Reflections	1462 [Rint = 0.0916]	2398 [Rint = 0.0789]	6181 [Rint = 0.0732]	8004 [Rint = 0.0784]
Data/restrains/parameters	1462 / 0 / 66	2398 / 0 / 86	6181 / 9 / 176	8004 / 7 / 212
Final *R* Indices [I>2σ(I)]	Robs = 0.0473 wRobs = 0.0519	Robs = 0.0311 wRobs = 0.0329	Robs = 0.0533 wRobs = 0.1129	Robs = 0.0471 wRobs = 0.0966
R indices [all data]	Rall = 0.0652 wRall = 0.0546	Rall = 0.0451 wRall = 0.0349	Rall = 0.0668 wRall = 0.1180	Rall = 0.0739 wRall = 0.1038
Fourier Difference max and min ($e·Å^{-3}$)	5.39 and -1.85	4.77 and -1.24	4.78 and -1.72	2.15 and -2.25

[a] $R = \sum \| F_o| - |F_c| / \sum |F_o|, wR = \{\sum [w(|F_o|^2 - |F_c|^2)^2] / \sum [w(|F^\circ|^4)^{1/2}$ and $w = 1/(\sigma^2(I) + 0.0004I^2)$.

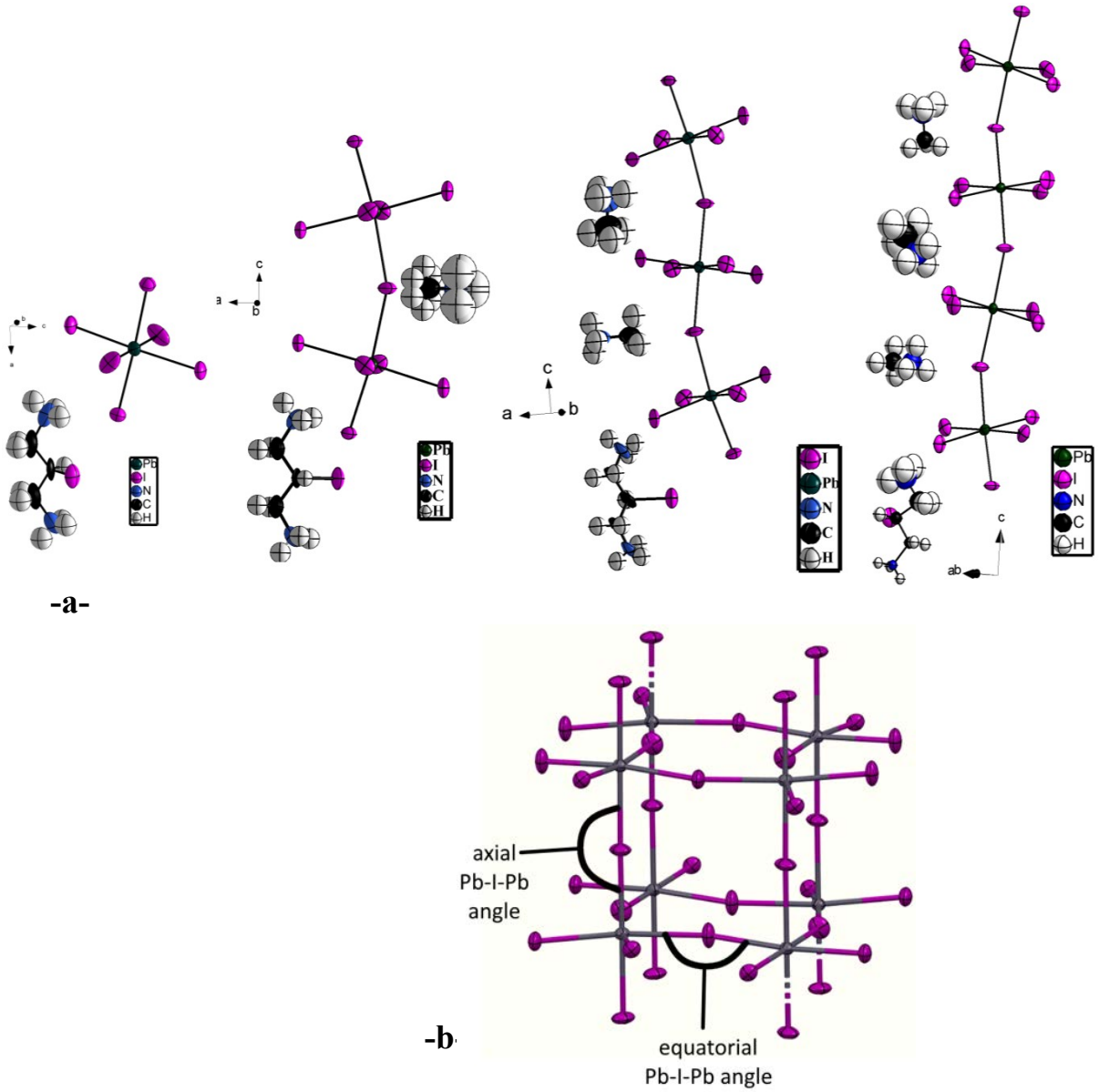

Fig. S3. -a- Part of the structures of $(DicI)(MA)_{n-1}Pb_nI_{3n+1}$ (n=1 to 4, from left to right) showing ADPs **; -b-** Definition of axial and equatorial Pb−I−Pb angles in the crystal structures of $(DicI)(MA)_{n-1}Pb_nI_{3n+1}$

Table S2. Selected bond distances for $(DicI)(MA)_{n-1}Pb_nI_{3n+1}$

$(DicI)PbI_4$		**$(DicI)(MA)Pb_2I_7$**		**$(DicI)(MA)_2Pb_3I_{10}$**		**$(DicI)(MA)_3Pb_4I_{13}$**	
Label	Distances (Å)	Label	Distances (Å)	Label	Distances (Å)	Label	Distances (Å)
Pb(1)-I(1)	3.2250(7)	Pb(1)-I(1)	3.0696(8)	Pb(1)- I(1)	3.182(2)	Pb(1)-I(1)	3.187(5)
Pb(1)-I(2)	3.1529(11)	Pb(1)-I(2)	3.2310(6)	Pb(1)-I(5)	3.039(4)	Pb(1)-I(1)	3.174(5)
Pb(1)-I(3)	3.1736(18)	Pb(1)-I(3)	3.1902(8)	Pb(1)-I(7)	3.337(4)	Pb(1)-I(2)	3.1540(17)
		Pb(1)-I(4)	3.1897(6)	Pb(1)- I(13)	3.242(2)	Pb(1)-I(6)	3.1749(17)
		Pb(1)-I(5)	3.2733(5)	Pb(1)-I(8)	3.174(4)	Pb(1)-I(10)	3.2329(5)
				Pb(1)-I(8)	3.196(4)	Pb(1)-I(11)	3.1369(10)
				Pb(2)- I(3)	3.154(3)	Pb(2)-I(4)	3.2432(18)
				Pb(2)-I(4)	3.200(5)	Pb(2)-I(5)	3.189(4)
				Pb(2)-I(7)	3.150(5)	Pb(2)-I(5)	3.172(4)
				Pb(2)-I(10)	3.1764(13)	Pb(2)-I(7)	3.1860(18)
				Pb(2)-I(10)	3.1929(13)	Pb(2)-I(9)	3.0419(13)
				Pb(2)-I(12)	3.177(3)	Pb(2)-I(11)	3.3297(10)
				Pb(3)- I(2)	3.243(3)	Pb(3)-I(13)	3.1801(18)
				Pb(3)-I(4)	3.269(4)	Pb(3)-I(14)	3.2523(18)
				Pb(3)-I(6)	3.069(4)	Pb(3)-I(18)	3.188(4)
				Pb(3)-I(11)	3.187(4)	Pb(3)-I(18)	3.174(4)
				Pb(3)-I(11)	3.182(2)	I(3)-Pb(3)	3.3045(10)
				Pb(3)-I(14)	3.184(2)	I(8)-Pb(3)	3.0513(13)
						I(3)-Pb(4)	3.1463(10)
						I(10)-Pb(4)	3.1837(5)
						Pb(4)-I(15)	3.1578(17)
						Pb(4)-I(16)	3.1654(17)
						Pb(4)-I(17)	3.179(6)
						Pb(4)-I(17)	3.182(6)
Average	3.1838		3.1908		3.1863		3.1827

Table S3. Selected bond angles for the $(DicI)(MA)_{n-1}Pb_nI_{3n+1}$ compounds

	$(DicI)PbI_4$	**$(DicI)(MA)Pb_2I_7$**		**$(DicI)(MA)_2Pb_3I_{10}$**		**$(DicI)(MA)_3Pb_4I_{13}$**	
Label	Angle (°) Axial	Label	Angle (°) Axial	Label	Angle (°) Axial	Label	Angle (°) Axial
		Pb(1)-I(5)-Pb(1)	158.20(10)	Pb(1)-I(7)-Pb(2)	158.49	Pb(2)-I(11)-Pb(1)	158.78
				Pb(2)-I(4)-Pb(3)	158.93	Pb(1)-I(10)-Pb(4)	160.28
						Pb(4)-I(3)-Pb(3)	159.17
Average			158.20(10)		158.71		159.41
Label	Angle (°) Equatorial	Label	Angle (°) Equatorial	Label	Angle (°) Equatorial	Label	Angle (°) Equatorial
Pb(1)-I(3)-Pb(1)	180	Pb(1)-I(3)-Pb(1)	178.74(25)	Pb(2)-I(10)-Pb(2)	178.73	Pb(1)-I(1)-Pb(1)	179.78
Pb(1)-I(1)-Pb(1)	143.47(7)	Pb(1)-I(4)-Pb(1)	149.75(10)	Pb(3)-I(11)-Pb(3)	179.63	Pb(4)-I(17)-Pb(4)	178.73
		Pb(1)-I(2)-Pb(1)	146.50(10)	Pb(1)-I(8)-Pb(1)	178.48	Pb(3)-I(18)-Pb(3)	179.49
				Pb(3)-I(2)-Pb(3)	148.36	Pb(2)-I(5)-Pb(2)	178.69
				Pb(2)-I(3)-Pb(2)	157.61	Pb(1)-I(2)-Pb(1)	158.71
				Pb(2)-I(12)-Pb(2)	155.29	Pb(2)-I(4)-Pb(2)	149.16
				Pb(1)-I(3)-Pb(1)	148.95	Pb(4)-I(5)-Pb(4)	160.48
				Pb(1)-I(1)-Pb(1)	150.61	Pb(4)-I(16)-Pb(4)	156.12
				Pb(3)-I(14)-Pb(3)	150.75	Pb(2)-I(7)-Pb(2)	151.36
						Pb(3)-I(13)-Pb(3)	150.44
						Pb(3)-I(14)-Pb(3)	149.48
						Pb(1)-I(6)-Pb(1)	156.69
Average	161.47		158.33		160.93		162.43

C- Thermal and optical characterization

C1- Thermal characterization

Thermogravimetric analysis (TGA). A full set of data were adopted via Diamond TGA set up, which was purchased from Perkin Elmer Company. The TGA device consists of an electronic high accuracy weight scale, which is connected with a high temperature oven surrounding the supplement area. Data were measured in the 25-600 ℃ (n= 2), 25-800 ℃ (n= 1), 25-1000 ℃ (n= 2), under a continuous N_2 flow at a flow rate of 200 mL/min.

The thermogravimetric analysis curves are provided Figure S4. All the thermal diagrams exhibit very similar trends in the temperature regions of ~200℃ and ~400℃. The thermal decomposition starts at ~200 ℃, with the evaporation of the organic part. For n=1 (53.59%), this corresponds to ~1 (DicI) and 2HI, per formula unit and for n=2 (37.41%) and n=3 (31.53%), it corresponds to ~1(DicI) 3HI and MAI. At temperatures around 400℃, all diagrams display a significant mass loss of PbI_2. For n=1 (52.27%) this corresponds to ~1 PbI_2, per formula unit, while for n=2 (51.44%) and n=3 (60.01%), that corresponds to ~2 PbI_2 and ~3 PbI_2 per formula unit, respectively.

Differential Scanning Calorimetry (DSC). A full set of data were collected via DSC-250 for all n=1-3 compounds. Approximately 2.3 mg of each sample were placed in aluminum pans which were then hermetically closed. They were placed in the calorimeter along with an empty reference pan. The samples were first maintained in a 2 min isothermal state and then heated from 30 ℃ up to 170 ℃ with a rate of 10 $℃/min$. The samples then maintained in a 2 min isothermal state and then cooled from 170 ℃ down to 30 ℃ with a rate of 10 $℃/min$. The process was repeated twice, with the first cycle discarded as it was performed only to erase the samples thermal history.

The DSC diagrams for the 3 compounds are provided Figure S4. No endothermic nor exothermic peaks were observed in the 30℃-170℃ range meaning in particular that no phase transition takes place in the studied temperature range.

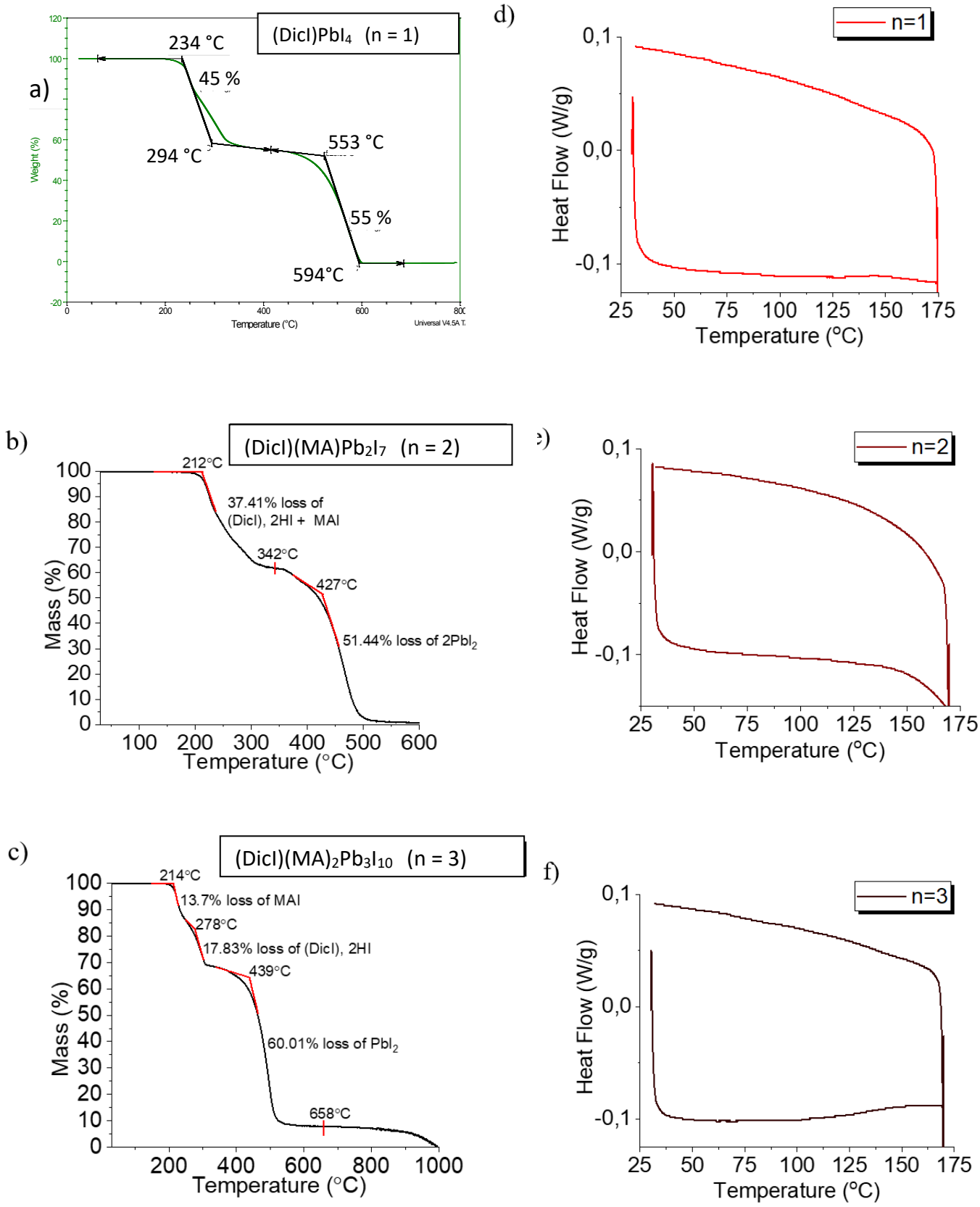

Fig. S4. Thermogravimetric analysis (TGA) (a-c) and Differential Scanning Calorimetry (DSC) diagrams (d-f) of the n=1, 2 and 3 compounds.

C2- Optical characterization

Optical Absorption Spectroscopy. Optical diffuse reflectance measurements were performed using a Shimadzu UV-2600 plus UV-vis-NIR spectrometer operating in the 185-1400 nm region using $BaSO_4$ as the reference of 100% reflectance. The optical band gap of the material was estimated by converting reflectance to absorption according to the Kubelka-Munk equation: $\frac{\alpha}{s} = \frac{(1-R)2}{2R}$, where R is the reflectance and α and S are the absorption and scattering coefficients[1] respectively.

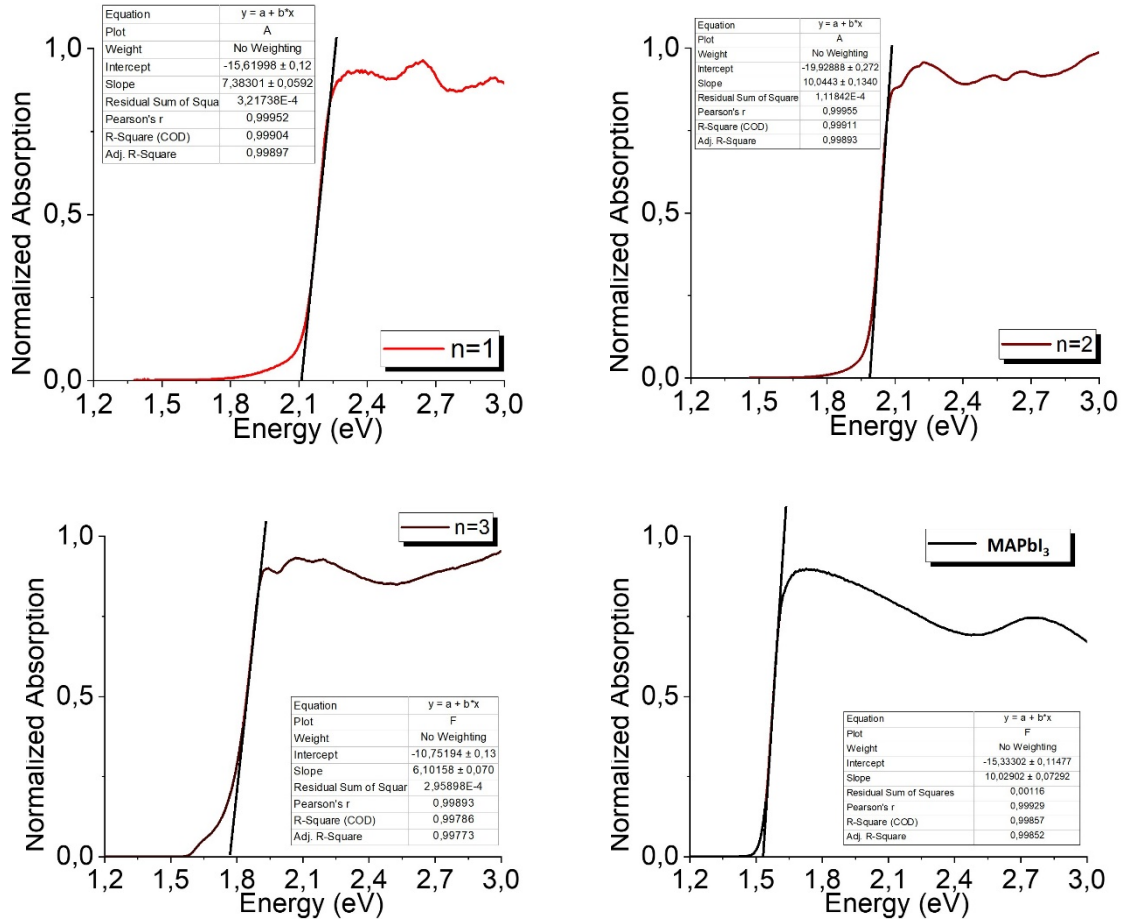

Fig. S5. Fitting of the absorption spectra leading to the optical values of 2.12 eV ((DicI)PbI_4 -n= 1-), 1.98 eV ((DicI)(MA)Pb_2I_7 -n= 2-), 1.76 eV ((DicI)$(MA)_2Pb_3I_{10}$ -n= 3-), and 1.53 eV ($MAPbI_3$).

Photoluminescence Spectroscopy (PL). Photoluminescence spectra were collected on oriented crystals of the $(Dic)(MA)_{n-1}Pb_nI_{3n+1}$ perovskites (n = 1-3) using Horiba LabRam Evolution high resolution confocal Raman microscope spectrometer (600 g/mm diffraction grating) equipped with a diode CW laser (532 nm, 35 mW) and a Synapse CCD camera. The incident laser beam was parallel to the (010) direction of the crystals and focused at ~1 μm spot size. Unless stated otherwise, the maximum power output of the laser source was filtered to 0.01% of the maximum power output.

D- Theoretical analyses and simulations

Lattice mismatch analysis. In the framework of the lattice mismatch model for multilayered 2D perovskites[5], the possible accumulation of strain within the perovskite lattice for intermediate n values is evaluated from the relative difference between the in-plane lattice parameters of the n=1 compound of the series and the lattice parameter of the 3D perovskite reference (here $MAPbI_3$). The evolution of the in-plane lattice parameter as a function of n, is characteristic of the strain relaxation in the lattice. Very large mismatches prevent systems from forming materials with high n values, as the accumulation of strain energy scales as the square of the lattice mismatch[5]. This situation is encountered in the PEA series, which exhibits a larger (negative) mismatch than the BA series (Figure S6). We may notice that the DJ 3AMP series presents a positive mismatch on the same order as the one of the BA series, leading also to the observation of multilayered compounds up to n=4. The new Dicl-based DJ series reported in the present work is in a favorable situation, with a limited negative lattice mismatch, explaining the possible formation of multilayered compounds up to n=4.

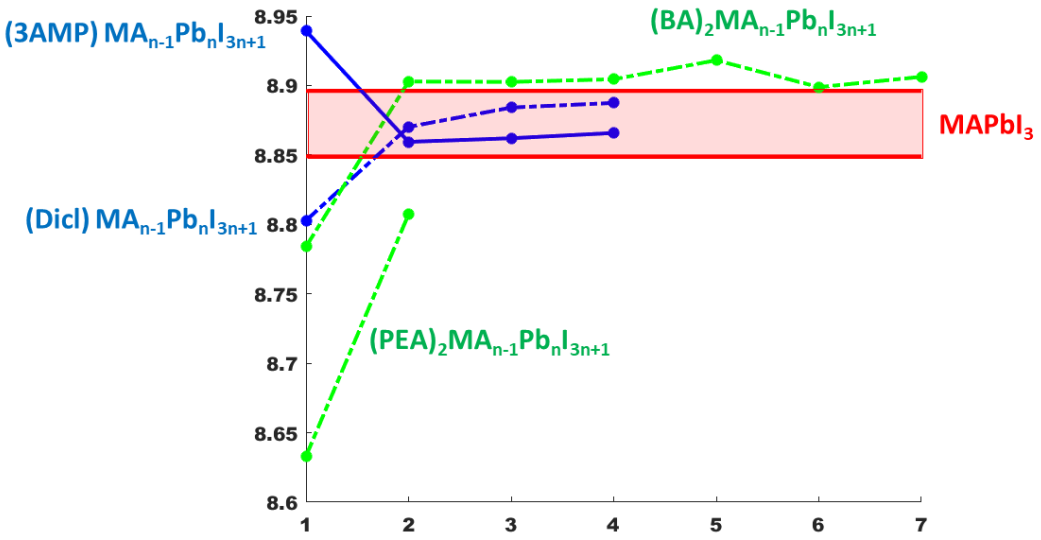

Fig. S6. Lattice mismatch analysis in multilayered 2D perovskites[5]. The evolution of the experimental room temperature in-plane average lattice parameter of classical RP (green dotted lines for BA and PEA series[6]) and DJ (blue continuous line for the 3AMP series[2]) multilayered perovskites. The blue dotted line is reported for the new Dicl series of the present work. The red area represents the typical lattice parameter range found experimentally for the reference 3D perovskite $MAPbI_3$[7, 8].

Band structure calculations. Periodic DFT calculations have been performed within the planewave/pseudopotential formalism, as implemented in the Quantum-Espresso suite[9, 10]. As reported in the main text, these are based on standard GGA method for the description of the exchange and correlation potential, as proposed by Perdue *et al.*,[11] and performed within the non-collinear spin description, with inclusion of spin-orbit-coupling. Energy cutoff for the planewave expansion of the single particle states and electronic density was set to 25 Ry and 200 Ry, respectively, along with ultrasoft pseudopotentials[12]. The present computational set-up was shown to provide good trade-off between accuracy and computational cost[13]. Periodic models from single-crystal XRD were used as reference for calculations. Van der Waals interactions were included using the DFT-D2 method[14], for the optimization of the atomic positions of the organic component. Due to similar in-plane lattice parameters for the various, we used same 3x3 automatic sampling of the Brillouin zone[15], for the reciprocal directions associated to the inorganic plane. Out of plane sampling instead reflected the length of the direct lattice parameter associated with the plane-stacking (final samplings corresponding to 3x3x2, for n=1,2,4 and n=3x3x1 for n=3).

Dielectric profile calculations. Dielectric profiles were calculated following the procedure in Ref. [16]. It consists in performing electronic structure calculations of periodic slabs of 2D halide perovskites and evaluating the variation of the electronic density following application of electric field (0.01 V/Å) along the plane stacking direction. Periodic DFT calculations are performed using atomic-centered, periodic DFT calculations, as implemented in the SIESTA code[17]. Core electrons are described with Troullier-Martins pseudopotentials[18], while the valence wavefunction is developed over a double-zeta polarized basis set of finite-range numerical pseudoatomic orbitals.

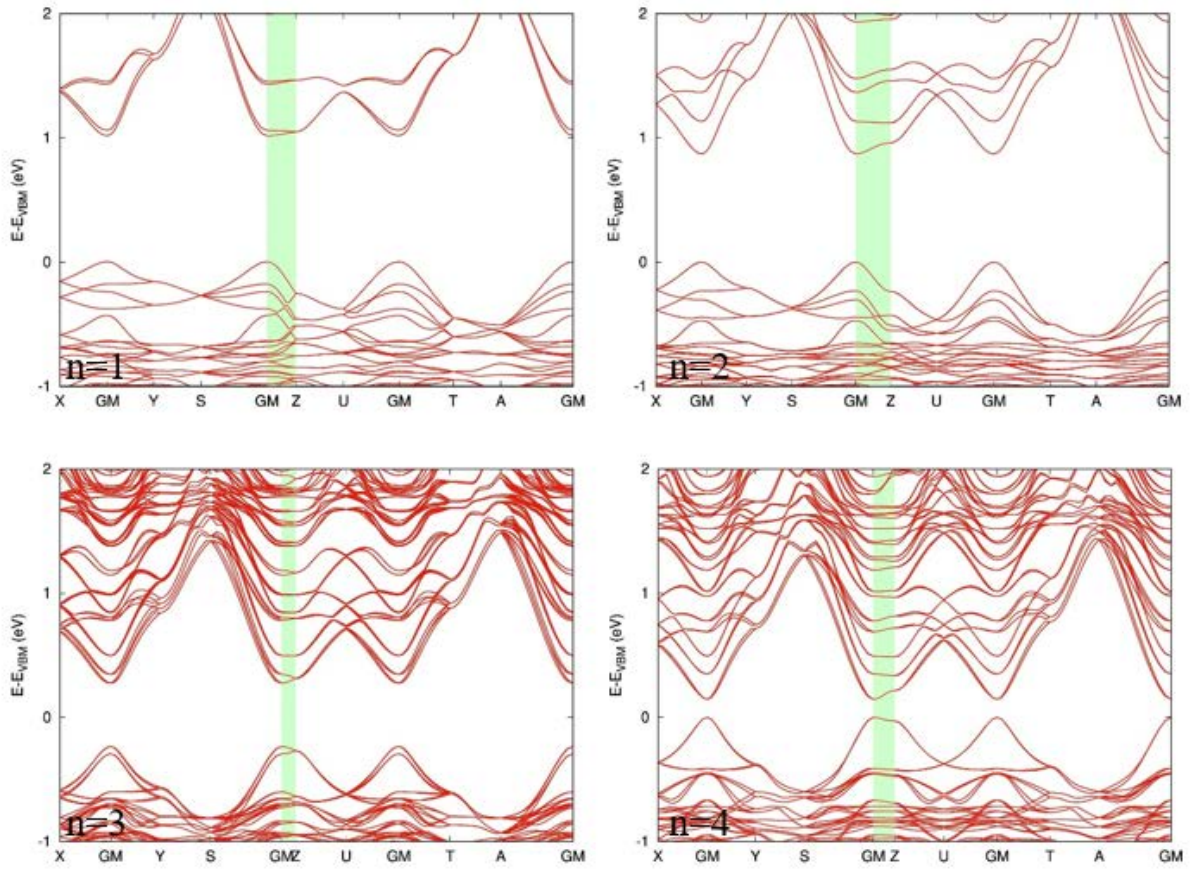

Fig. S7. Band structure dispersion for (DicI)$MA_{n-1}Pb_nI_{3n+1}$ (n=1,4) layered halide perovskites. All compounds discussed within primitive orthorhombic frame, with plane stacking axis oriented along z. This ease the comparison between different compounds. The highlighted region is associated to interlayer band dispersion.

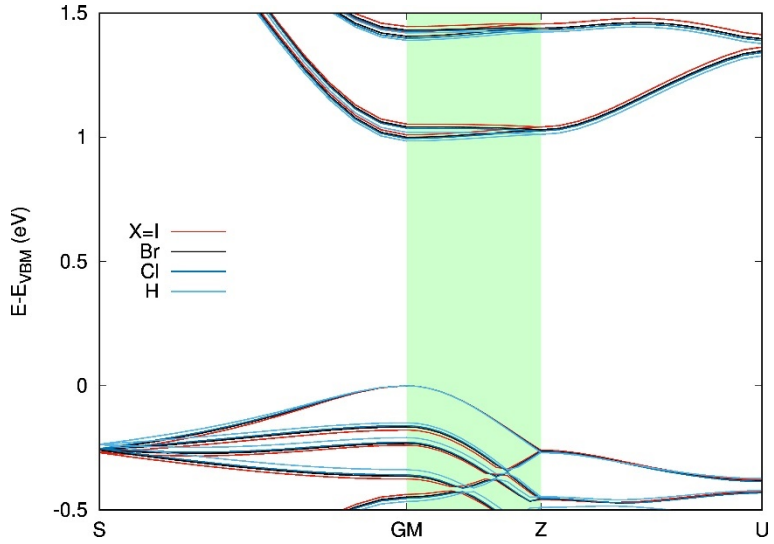

Fig. S8. Band structure dispersion for n=1, (DicI)PbI layered halide perovskites, with the iodine from the $(DicI)^{2+}$ spacer substituted by a bromine (Br), a chlorine (Cl) and a hydrogen (H).

Table S4. Effective masses along the plane stacking direction for 2D $A_mMA_nPb_nI_{3n+1}$ halide perovskites containing different spacers (BA, m=2 – 3AMP, m=1 – DicI, m=1). For DicI spacer, we consider hypothetical compounds where the iodine from the spacer is substituted by a hydrogen, a chlorine and a iodine

spacer	**n**		**hole**	**electron**
BA	1		Inf.	Inf.
3AMP			0.49	1.34
DicI		H	0.24	1.87
		Cl	0.24	1.48
		Br	0.25	1.51
		I	0.25	1.54
	2		0.22	0.51
	3		0.45	0.33
	4		0.43	0.23

References

1 A. A. Christy, O. M. Kvalheim, R. A. Velapoldi, *Vibrational Spectroscopy* **1995**, *9*, 19-27 https://doi.org/10.1016/0924-2031(94)00065-O.

2 L. Mao, W. Ke, L. Pedesseau, Y. Wu, C. Katan, J. Even, M. R. Wasielewski, C. C. Stoumpos, M. G. Kanatzidis, *Journal of the American Chemical Society* **2018**, *140*, 3775-3783 10.1021/jacs.8b00542.

3 L. Gao, X. Li, B. Traoré, Y. Zhang, J. Fang, Y. Han, J. Even, C. Katan, K. Zhao, S. Liu, M. G. Kanatzidis, *Journal of the American Chemical Society* **2021**, *143*, 12063-12073 10.1021/jacs.1c03687.

4 C. C. Stoumpos, D. H. Cao, D. J. Clark, J. Young, J. M. Rondinelli, J. I. Jang, J. T. Hupp, M. G. Kanatzidis, *Chemistry of Materials* **2016**, *28*, 2852-2867 10.1021/acs.chemmater.6b00847.

5 M. Kepenekian, B. Traore, J.-C. Blancon, L. Pedesseau, H. Tsai, W. Nie, C. C. Stoumpos, M. G. Kanatzidis, J. Even, A. D. Mohite, S. Tretiak, C. Katan, *Nano Letters* **2018**, *18*, 5603-5609 10.1021/acs.nanolett.8b02078.

6 M. A. K. Sheikh, D. Kowal, M. H. Mahyuddin, R. Cala', E. Auffray, M. E. Witkowski, M. Makowski, W. Drozdowski, H. Wang, C. Dujardin, D. Cortecchia, M. D. Birowosuto, *The Journal of Physical Chemistry C* **2023**, *127*, 10737-10747 10.1021/acs.jpcc.3c00824.

7 Q. Dong, Y. Fang, Y. Shao, P. Mulligan, J. Qiu, L. Cao, J. Huang, *Science* **2015**, *347*, 967-970 10.1126/science.aaa5760.

8 C. C. Stoumpos, C. D. Malliakas, M. G. Kanatzidis, *Inorg Chem* **2013**, *52*, 9019-38 10.1021/ic401215x.

9 P. Giannozzi, S. Baroni, N. Bonini, M. Calandra, R. Car, C. Cavazzoni, D. Ceresoli, G. L. Chiarotti, M. Cococcioni, I. Dabo, A. Dal Corso, S. de Gironcoli, S. Fabris, G. Fratesi, R. Gebauer, U. Gerstmann, C. Gougoussis, A. Kokalj, M. Lazzeri, L. Martin-Samos, N. Marzari, F. Mauri, R. Mazzarello, S. Paolini, A. Pasquarello, L. Paulatto, C. Sbraccia, S. Scandolo, G. Sclauzero, A. P. Seitsonen, A. Smogunov, P. Umari, R. M. Wentzcovitch, *Journal of Physics: Condensed Matter* **2009**, *21*, 395502 10.1088/0953-8984/21/39/395502.

10 P. Giannozzi, O. Andreussi, T. Brumme, O. Bunau, M. Buongiorno Nardelli, M. Calandra, R. Car, C. Cavazzoni, D. Ceresoli, M. Cococcioni, N. Colonna, I. Carnimeo, A. Dal Corso, S. de Gironcoli, P. Delugas, R. A. DiStasio, A. Ferretti, A. Floris, G. Fratesi, G. Fugallo, R. Gebauer, U. Gerstmann, F. Giustino, T. Gorni, J. Jia, M. Kawamura, H. Y. Ko, A. Kokalj, E. Küçükbenli, M. Lazzeri, M. Marsili, N. Marzari, F. Mauri, N. L. Nguyen, H. V. Nguyen, A. Otero-de-la-Roza, L. Paulatto, S. Poncé, D. Rocca, R. Sabatini, B. Santra, M. Schlipf, A. P. Seitsonen, A. Smogunov, I. Timrov, T. Thonhauser, P. Umari, N. Vast, X. Wu, S. Baroni, *Journal of Physics: Condensed Matter* **2017**, *29*, 465901 10.1088/1361-648X/aa8f79.

11 J. P. Perdew, K. Burke, M. Ernzerhof, *Physical review letters* **1996**, *77*, 3865.

12 D. Vanderbilt, *Physical Review B* **1990**, *41*, 7892-7895 10.1103/PhysRevB.41.7892.

13 C. Quarti, E. Mosconi, F. De Angelis, *Chemistry of Materials* **2014**, *26*, 6557-6569 10.1021/cm5032046.

14 S. Grimme, *Journal of Computational Chemistry* **2004**, *25*, 1463-1473 https://doi.org/10.1002/jcc.20078.

15 H. J. Monkhorst, J. D. Pack, *Physical review B* **1976**, *13*, 5188.

16 J. Even, L. Pedesseau, M. Kepenekian, *Physical Chemistry Chemical Physics* **2014**, *16*, 25182-25190 10.1039/C4CP03267E.

17 M. S. José, A. Emilio, D. G. Julian, G. Alberto, J. Javier, O. Pablo, S.-P. Daniel, *Journal of Physics: Condensed Matter* **2002**, *14*, 2745 10.1088/0953-8984/14/11/302.

18 N. Troullier, J. L. Martins, *Physical Review B* **1991**, *43*, 1993-2006 10.1103/PhysRevB.43.1993.